

Stunted accretion growth of black holes by combined effect of the flow angular momentum and radiation feedback

Kazuyuki Sugimura,^{1*} Takashi Hosokawa,² Hidenobu Yajima,^{1,3}
Kohei Inayoshi⁴ and Kazuyuki Omukai¹

¹*Astronomical Institute, Tohoku University, Aoba, Sendai 980-8578, Japan*

²*Department of Physics, Kyoto University, Sakyo, Kyoto 606-8502, Japan*

³*Frontier Research Institute for Interdisciplinary Sciences, Tohoku University, Aoba, Sendai 980-8578, Japan*

⁴*Department of Astronomy, Columbia University, 550 W. 120th Street, New York, NY 10027, USA*

19 August 2021

ABSTRACT

Accretion on to seed black holes (BHs) is believed to play a crucial role in formation of supermassive BHs observed at high-redshift ($z > 6$). Here, we investigate the combined effect of gas angular momentum and radiation feedback on the accretion flow, by performing 2D axially symmetric radiation hydrodynamics simulations that solve the flow structure across the Bondi radius and the outer part of the accretion disc simultaneously. The accreting gas with finite angular momentum forms a rotationally-supported disc inside the Bondi radius, where the accretion proceeds by the angular momentum transport due to assumed α -type viscosity. We find that the interplay of radiation and angular momentum significantly suppresses accretion even if the radiative feedback is weakened in an equatorial shadowing region. The accretion rate is $O(\alpha) \sim O(0.01 - 0.1)$ times the Bondi value, where α is the viscosity parameter. By developing an analytical model, we show that such a great reduction of the accretion rate persists unless the angular momentum is so small that the corresponding centrifugal radius is $\lesssim 0.04$ times the Bondi radius. We argue that BHs are hard to grow quickly via rapid mass accretion considering the angular momentum barrier presented in this paper.

Key words: quasars: supermassive black holes-cosmology: theory.

1 INTRODUCTION

Observations of supermassive black holes (SMBHs) with mass $\sim 10^9 M_\odot$ at redshift $z \gtrsim 6$, or $\lesssim 1$ Gyr after the big bang, severely constrain their formation mechanism (e.g., Fan et al. 2001; Willott et al. 2010; Mortlock et al. 2011; Venemans et al. 2013; Wu et al. 2015; see also Gallerani et al. 2017 for review). Heavy seed BHs have been invoked in several scenarios to reconcile the short available time with their hugeness (see, e.g., Volonteri 2012; Haiman 2013, for a review), which includes (1) Pop III remnant BHs with mass of $M_{\text{BH}} \lesssim 10^3 M_\odot$ (e.g., Yoshida et al. 2008; Hosokawa et al. 2011, 2016; Susa et al. 2014; Hirano et al. 2015; Stacy et al. 2016); (2) direct collapse BHs with $M_{\text{BH}} \sim 10^5 M_\odot$ formed via the collapse of supermassive stars (e.g., Omukai 2001; Bromm & Loeb 2003; Hosokawa et al. 2012; Sugimura et al. 2014, 2016; Inayoshi et al. 2014; Chon et al. 2016; Umeda et al. 2016); and (3) massive BHs with $M_{\text{BH}} \sim 10^3 M_\odot$

formed as a consequence of stellar mergers in dense clusters (e.g., Omukai et al. 2008; Devecchi & Volonteri 2009; Katz et al. 2015; Tagawa et al. 2015; Yajima & Khochfar 2016; Sakurai et al. 2017).

In all the cases, the seeds have to increase their mass further by several orders of magnitude. Although Pop III remnants with relatively small mass have been claimed to become SMBHs by $z \gtrsim 6$ by very rapid (super-Eddington) gas accretion (Volonteri & Rees 2005; Madau et al. 2014; Alexander & Natarajan 2014; Volonteri et al. 2015), whether this actually occurs or not is still very uncertain. This is because our knowledge on the realistic accretion process is still limited.

Bondi (1952) analytically investigated the most simplistic case of steady, spherical accretion of the polytropic gas from a homogeneous and static medium (see also, e.g., Shapiro & Teukolsky 1983). For a BH with mass M_{BH} surrounded by a gas with density ρ_∞ and sound speed $c_{s,\infty}$,

* E-mail: sugimura@astr.tohoku.ac.jp

the so-called Bondi accretion rate is

$$\dot{M}_B = \frac{4\pi\lambda_B\rho_\infty G^2 M_{\text{BH}}^2}{c_{s,\infty}^3} = 1.7 \times 10^{-3} \left(\frac{\lambda_B}{1.12} \right) \times \left(\frac{n_{\text{H},\infty}}{10^5 \text{ cm}^{-3}} \right) \left(\frac{M_{\text{BH}}}{10^3 M_\odot} \right)^2 \left(\frac{c_{s,\infty}}{8 \text{ km s}^{-1}} \right)^{-3} M_\odot \text{ yr}^{-1}. \quad (1)$$

Here, λ_B is the non-dimensional factor depending on the polytropic index γ ($\lambda_B = 1.12$ for the isothermal, i.e., $\gamma = 1$, case) and $c_{s,\infty} = 8 \text{ km s}^{-1}$ for a neutral primordial gas with temperature $T = 10^4 \text{ K}$. In the second expression of Eq. (1), we use the relation between the number density of hydrogen atoms $n_{\text{H},\infty}$ and ρ_∞ for the primordial gas.

Although the Bondi rate provides a rough estimate of an accretion rate onto a BH, various effects reduce the rate in realistic situations. For instance, radiation feedback from circum-BH discs can significantly disturb the accretion flow so that the rate decreases down to $\lesssim 0.01\dot{M}_B$ (e.g., Milosavljević et al. 2009; Park & Ricotti 2011, 2012; Park et al. 2017). Recent studies have proposed pathways to alleviate the feedback, in such cases as where the radiation is highly obscured around the equatorial plane by disc winds (Sugimura et al. 2017; Takeo et al. 2018) or where the radiation is trapped in a dense (super-Eddington) accretion flow (Inayoshi et al. 2016; Sakurai et al. 2016). These studies, however, do not consider the effect of angular momentum on the large-scale accretion flow, assuming that the size of the circum-BH disc is much smaller than the Bondi radius. This assumption may not be always the case. We need to know the condition that the effect of angular momentum becomes significant.

Accretion to active galactic nuclei (AGNs) has been investigated in the last few decades (e.g., Ciotti & Ostriker 2001; Wada & Norman 2002; Kawakatu & Wada 2008; Kurosawa & Proga 2009; Novak et al. 2011; Kawaguchi & Mori 2010; Barai et al. 2012; Yuan et al. 2012). In such a context, the effect of gas angular momentum has partly been investigated. Even without radiation feedback, moderate gas angular momentum significantly suppresses the accretion in low-luminosity AGN (Proga & Begelman 2003b,a; Cuadra et al. 2006; Li et al. 2013; Gaspari et al. 2015; Inayoshi et al. 2018). This implies that the effect of angular momentum, as well as radiation feedback, needs to be considered in studying the accretion on to the seed BHs. In Begelman & Volonteri (2017), they have studied the properties of super-Eddington accretion flows for cases where the disc size is smaller than the photon-trapping radius. In contrast, we are interested in cases where the disc is much larger than the photon-trapping radius, which is far smaller than the Bondi radius.

In this work, to see the combined effect of the angular momentum and the radiation feedback on seed BH accretion, we perform a set of 2D axisymmetric radiation hydrodynamics simulations, considering both finite gas angular momentum and radiation from the circum-BH discs. We follow formation of rotationally-supported discs and subsequent viscous accretion through them. We find that angular momentum of the gas, in cooperation with radiation feedback, suppresses the accretion on to seed BHs. To understand its mechanism, we also develop an analytical model for accretion from a rotating medium.

The paper is organized as follows. In Sec. 2, we describe the numerical method and the parameter sets explored. In Sec. 3, we present the results of our simulations. In Sec. 4, we develop an analytical model, which allows us to obtain the

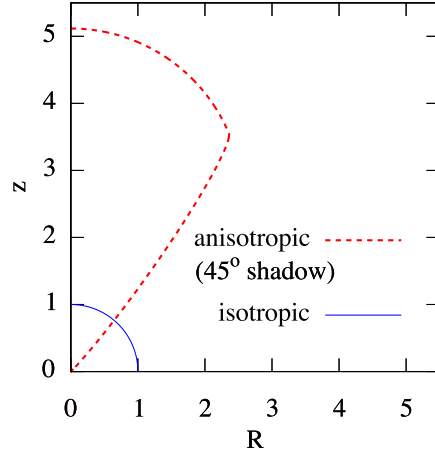


Figure 1. Directional dependence of ionizing flux. The radial extent represents the strength of the flux compared to the isotropic case.

condition for suppression of accretion. In Sec. 5, we discuss the possible growth history of Pop III remnant BHs based on our findings, as well as the caveats of our simulations. Finally, we summarize in Sec. 6.

2 METHOD

We perform axisymmetric 2D radiation hydrodynamics (RHD) simulations, by using a modified version of a public grid-based multidimensional magnetohydrodynamics (MHD) code PLUTO 4.1 (Mignone et al. 2007), which is mostly the same as used in our previous work (Sugimura et al. 2017; see also Kuiper et al. 2010a,b, 2011; Kuiper & Klessen 2013; Hosokawa et al. 2016). Major update here is implementation of physics related to the rotation of gas. In the rest of this paper, we use both spherical (r, θ, ϕ) and cylindrical (R, z, ϕ) coordinates interchangeably, although the spherical one was actually used in the calculation.

2.1 Modelling accretion on to a BH under radiation feedback

We briefly describe the basic properties of the code that are common to our previous work (see Sugimura et al. 2017, for details). With this code, we follow BH accretion from a homogeneous surrounding medium under radiation feedback.

We put a BH at the centre of computational domain and treat it as a sink. Through the sink surface, the gas is allowed to flow in, while the radiation is emitted according to a semi-analytical model described below. We solve the coupled equations of hydrodynamics, radial multi-frequency radiation transport and primordial gas chemistry. In the current version of the code, helium ionization is considered, hydrogen molecules are assumed to be completely destroyed, and the self-gravity of gas is ignored.

We consider ionizing photons emitted from the circum-BH discs with a semi-analytical prescription. Using the accretion rate \dot{M} evaluated at the sink surface, the luminosity

L is given by (Watarai et al. 2000)

$$L = \begin{cases} 2 L_E [1 + \ln(\dot{m}/20)] & \dot{m} > 20 \\ 0.1 L_E \dot{m} & \dot{m} < 20 \end{cases}, \quad (2)$$

with $\dot{m} \equiv \dot{M}/\dot{M}_E$. Here, L_E is the Eddington luminosity,

$$L_E = \frac{4\pi G M_{\text{BH}} c m_{\text{p}}}{\sigma_{\text{T}}} = 3.3 \times 10^7 \left(\frac{M_{\text{BH}}}{10^3 M_{\odot}} \right) L_{\odot}, \quad (3)$$

and \dot{M}_E the (efficiency-independent) Eddington accretion rate,

$$\dot{M}_E = \frac{L_E}{c^2} = 2.2 \times 10^{-6} \left(\frac{M_{\text{BH}}}{10^3 M_{\odot}} \right) M_{\odot} \text{ yr}^{-1}. \quad (4)$$

Note that the decrease of radiative efficiency at $\dot{M} \gg \dot{M}_E$ is caused by photon trapping in the slim discs (Abramowicz et al. 1988). We assume that the spectral energy distribution is given by the power law $L_{\nu} \propto \nu^{-1.5}$ with the frequency minimum at $h\nu_{\text{min}} = 13.6 \text{ eV}$ and that $L = \int_{\nu_{\text{min}}}^{\infty} L_{\nu} d\nu$ (e.g., Park & Ricotti 2011).

Radiation from the sink is supposed to be anisotropic, partly because the photons from the hot inner part of the circm-BH disc is obscured by some outer materials. For example, Proga et al. (2000) suggested that line-driven winds from an SMBH accretion disc make a shadowing region with opening angle from the equatorial plane $\sim 10^{\circ}$. However, especially in the case with smaller BH mass or lower metallicity, the anisotropy is highly uncertain due to the lack of knowledge on obscuring materials, which are presumably (failed) winds or coroneae above the disc¹ (see, e.g., Begelman et al. 1983; Hollenbach et al. 1994; Woods et al. 1996; Proga et al. 2000; Wada 2012; Suzuki & Inutsuka 2014; Nomura et al. 2016). We thus do not attempt to realistically model the anisotropy, but instead, consider the two limiting cases: isotropic radiation and anisotropic radiation with a $\sim 45^{\circ}$ shadowing region (Fig. 1; Equation 9 of Sugimura et al. 2017). We expect the reality lies somewhere between the two.

2.2 Modelling gas rotation

We assume that the surrounding gas has the initial profile of specific angular momentum

$$j(\mathbf{x}) = \begin{cases} \left(\frac{R}{r_{\text{B}}} \right)^2 j_{\infty} & R < r_{\text{B}} \\ j_{\infty} & r_{\text{B}} < R \end{cases}, \quad (5)$$

with the Bondi radius

$$r_{\text{B}} = \frac{GM_{\text{BH}}}{c_{\text{s},\infty}^2} = 1.4 \times 10^4 \left(\frac{M_{\text{BH}}}{10^3 M_{\odot}} \right) \left(\frac{c_{\text{s},\infty}}{8 \text{ km s}^{-1}} \right)^{-2} \text{ au}. \quad (6)$$

That is, the gas has constant j throughout the computational domain, except near the rotation axis with $R < r_{\text{B}}$, where the angular velocity $\Omega = j/R^2$ is constant instead. Below, we interchangeably use j and the centrifugal radius R_{c} , where the centrifugal force and the BH gravity balances,

to indicate the angular momentum of the accreted gas, as R_{c} is related to j as

$$R_{\text{c}} = \frac{j^2}{GM_{\text{BH}}}. \quad (7)$$

Angular momentum must be transported for a gas with finite j to reach the vicinity of the BH. We assume the α -type viscous stress (Shakura & Sunyaev 1973; see also Igumenshchev & Abramowicz 1999; Stone et al. 1999; Li et al. 2013), which is possibly due to turbulence driven by the magnetorotational instability (MRI; Balbus & Hawley 1998). The gravitational torque is insignificant in the cases studied here, because the disc is highly gravitationally stable (see Appendix E). Note that while the value of α corresponding to the actual MRI turbulence is yet to be fully understood, Bai & Stone (2013), for example, have reported that α is ~ 0.01 – 0.02 in the case with a weak vertical magnetic field but can be even larger than unity in the strong field case.

To assure that the viscosity works only inside the disc (e.g., Stone et al. 1999), we introduce a confinement factor f and use the following expression for viscosity:²

$$\nu = f \left(\frac{\Omega}{\Omega_{\text{K}}} \right) \frac{\alpha \gamma c_{\text{s}}^2}{\Omega_{\text{K}}}, \quad (8)$$

with isothermal sound speed c_{s} , adiabatic index $\gamma = 5/3$ and Keplerian angular velocity $\Omega_{\text{K}} = \sqrt{GM_{\text{BH}}/R^3}$. Here, we identify the disc region based on the degree of rotational support against the BH gravity: we set $f = 0$ for $\Omega/\Omega_{\text{K}} < \tilde{\Omega}_{\text{th}}$ and $f = 1$ for $\tilde{\Omega}_{\text{th}} + \Delta\tilde{\Omega} < \Omega/\Omega_{\text{K}}$, and linearly interpolate between them, with the threshold value $\tilde{\Omega}_{\text{th}} = 0.8$ and the transition width $\Delta\tilde{\Omega} = 0.1$ in most of our calculations. We check the effect of changing $\tilde{\Omega}_{\text{th}}$ in Sec. A2. Note that we have seen in test runs that if the viscosity is not limited to the disc, the disc will disappear and the flow becomes spherical due to angular momentum transport in the entire computational domain.

2.3 Cases considered

Our runs are summarized in Table 1. In all runs, we set $M_{\text{BH}} = 10^3 M_{\odot}$ and fix it constant during the calculations. The surrounding medium is assumed to be the neutral primordial gas with density $n_{\text{H},\infty} = 10^5 \text{ cm}^{-3}$ and temperature $T_{\infty} = 10^4 \text{ K}$. In the fiducial run, we assume anisotropic radiation field with $\alpha = 0.01$ and $R_{\text{c},\infty} \equiv j_{\infty}^2/GM_{\text{BH}} = 0.1 r_{\text{B}}$. In order to examine the parameter dependence, we study cases with different parameters of $(\alpha, R_{\text{c},\infty}/r_{\text{B}}) = (0.01, 0.03), (0.1, 0.1)$ and $(0.01, 0.3)$. For comparison, we also solve the flow structure under the isotropic radiation field with the similar parameter sets.

We start from the homogeneous and quasi-static ($v_r = v_{\theta} = 0$) initial condition. We turn the radiation off for the first $2 \times 10^5 \text{ yr}$ to allow the flow to settle in a steady state with a rotationally-supported disc. Note that this period is longer than either the dynamical time at r_{B} , $t_{\text{B}} = \Omega_{\text{K}}^{-1}(r_{\text{B}}) \sim 10^4 \text{ yr}$, or the viscous time at $R_{\text{c},\infty}$, $t_{\text{visc,c}} = R_{\text{c},\infty}^2/\nu(R_{\text{c},\infty}) \sim 10^5 (\alpha/0.01)^{-1} (R_{\text{c},\infty}/0.1 r_{\text{B}})^{1/2} \text{ yr}$.

¹ Note that the anisotropy generated in this way exists independently of the self-shielding effect in slim discs.

² Equation (8) can also be written as $\nu = f \alpha c_{\text{s,ad}}^2/\Omega_{\text{K}}$, with adiabatic sound speed $c_{\text{s,ad}} = \sqrt{\gamma} c_{\text{s}}$.

Table 1. Summary of runs.

$R_{c,\infty}/r_B$	α	radiation	t_{end} [yr]	$\dot{M}/\dot{M}_B^{c,d}$
0.1	0.01	anisotropic ^a	1.2×10^6	2.9×10^{-3}
0.1	0.1	anisotropic ^a	1.2×10^6	5.2×10^{-2}
0.3	0.01	anisotropic ^a	1.2×10^6	1.2×10^{-3}
0.03	0.01	anisotropic ^a	1.2×10^6	4.3×10^{-1}
0.1	0.01	isotropic	4×10^5	1.1×10^{-4}
0.1	0.1	isotropic	4×10^5	2.6×10^{-4}
0.3	0.01	isotropic	4×10^5	9.7×10^{-5}
0.1	0.01	no	2×10^5	4.1×10^{-2}
0.1	0.1	no	2×10^5	1.2×10^{-1}
0.3	0.01	no	2×10^5	3.4×10^{-2}
0.03	0.01	no	2×10^5	8.1×10^{-1}
Non-rotating case ^b				
0	—	anisotropic ^a	2×10^6	5.9×10^{-1}
0	—	isotropic	5×10^5	1.7×10^{-3}
0	—	no	—	1

NOTES.—We set $M_{\text{BH}} = 10^3 M_\odot$, $n_{\text{H},\infty} = 10^5 \text{ cm}^{-3}$ and $T_\infty = 10^4 \text{ K}$ in all runs.

^a Anisotropic radiation with $\sim 45^\circ$ shadow.

^b Results from analytical estimate and the simulations in Sugimura et al. (2017).

^c Accretion rate at the end of simulation (averaged near the end of simulation if oscillating).

^d The accretion rate can also be normalized by \dot{M}_E using the relation $\dot{M}/\dot{M}_E \approx 800\dot{M}/\dot{M}_B$ (See Eqs. 1 and 4).

We then turn on the radiation and follow the evolution until $t_{\text{end}} = 1.2 \times 10^6 \text{ yr}$ in the anisotropic radiation runs and $4 \times 10^5 \text{ yr}$ in the isotropic radiation runs.

We impose the reflection symmetry with respect to the equatorial plane, as well as axisymmetry around the rotation axis, and thus θ extends from 0° to 90° . In the r -direction, our computational domain ranges from $r_{\text{in}} = 10^{-2} r_B$ to $r_{\text{out}} = 10^2 r_B$. Note that r_{in} is smaller than either $R_{c,\infty} \sim 10^{-1} r_B$ (see above) or the Bondi radius for H II gas $r_{\text{B,HII}} \sim 10^{-1} r_B$ with $\sim 7 \times 10^4 \text{ K}$, while r_{out} is larger than the size of H II region. We use logarithmic grids in the r direction and homogeneous ones in the θ directions, with $N_r \times N_\theta = 512 \times 144$. We discuss the dependence of our results on the numerical configuration in Appendix D.

At the outer boundary, we let the flow go out from the computational domain but not come into it. At the inner boundary, we impose the same boundary condition in most cases, but when the gas is judged to belong to the Keplerian accretion disc (specifically, when $v_{r,\text{in}} < 0$ and $\Omega_{\text{in}} > 0.95 \Omega_{\text{K,in}}$, where quantities with subscripts “in” are evaluated at r_{in}), we determine the physical quantities in the ghost cells according to the radial profile of the isothermal Keplerian disc: $\rho = (r/r_{\text{in}})^{-3} \rho_{\text{in}}$, $p = (r/r_{\text{in}})^{-3} p_{\text{in}}$, $v_r = (r/r_{\text{in}})^{1/2} v_{r,\text{in}}$, $v_\phi = (r/r_{\text{in}})^{-1/2} v_{\phi,\text{in}}$ and $\mathcal{Q} = \mathcal{Q}_{\text{in}}$ for the other variables (see Appendix A2). We set a temperature floor at $T_{\text{min}} = 10^4 \text{ K}$ for simplicity (e.g., Sugimura et al. 2017), as well as minimum density $n_{\text{min}} = 10^{-1} \text{ cm}^{-3}$ and maximum velocity $v_{\text{max}} = 150 \text{ km/s}$ for numerical reasons. For the lowest angular momentum ($R_{c,\infty}/r_B = 0.03$) run, we additionally limit j to below j_∞ , because otherwise the disc accretes the gas with $j > j_\infty$, receiving additional angular momentum transported from the inner part of the

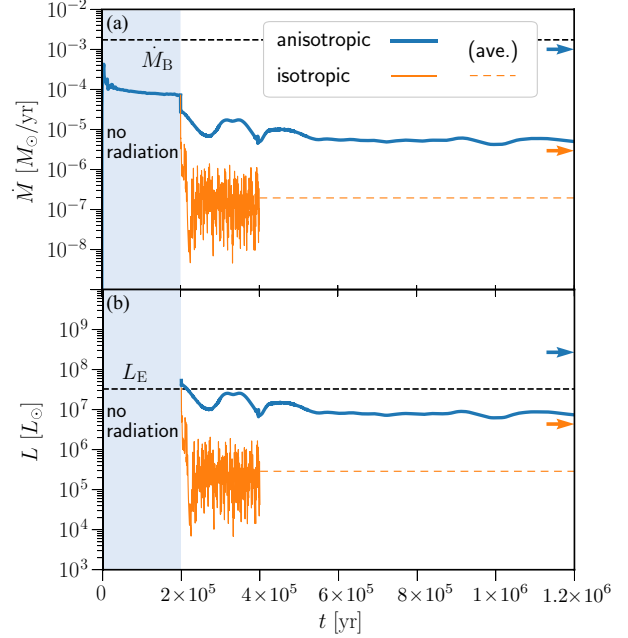


Figure 2. Time evolution of the (a) accretion rate and (b) luminosity in the runs with $\alpha = 0.01$ and $R_{c,\infty} = 0.1 r_B$. Both fiducial anisotropic radiation case (blue) and isotropic radiation case (orange) are shown. In these runs, the radiation is turned off for the initial 2×10^5 years. The bottom thin-dashed lines represent the averaged values for $3 \times 10^5 \text{ yr} < t < 4 \times 10^5 \text{ yr}$. The results for the non-rotating case (Sugimura et al. 2017) are also shown by arrows for comparison.

disc. Recall that our aim here is to study how the accretion flow structure varies with different j_∞ in a well controlled manner. We discuss how such a situation may be realized in Sec. 5.2 later. For the other higher angular momentum ($R_{c,\infty}/r_B \geq 0.1$) cases, we do not put the same upper limit on j because it hardly changes the result.

3 RESULTS

Results of our simulations are summarized in Table 1, along with our previous cases for the non-rotating gas (Sugimura et al. 2017), for comparison. Below, we first describe the fiducial anisotropic radiation run in Sec. 3.1. We then present the isotropic radiation run with the same parameter set in Sec. 3.2 and finally see the cases with different parameter sets in Sec. 3.3.

3.1 The fiducial run

We first describe the fiducial run, where the parameter set is given as follows: $M_{\text{BH}} = 10^3 M_\odot$, $n_{\text{H},\infty} = 10^5 \text{ cm}^{-3}$, $T_\infty = 10^4 \text{ K}$, $\alpha = 0.01$ and $R_{c,\infty} = 0.1 r_B$. The radiation field is assumed to be anisotropic with $\sim 45^\circ$ shadow (see Fig. 1). Such a wide obscuration can be regarded as an extreme of strong anisotropy. Starting from the homogeneous initial condition, we follow the evolution of flow with the radiation turned off until $2 \times 10^5 \text{ yr}$. We then turn on the radiation and follow the evolution until $t_{\text{end}} = 1.2 \times 10^6 \text{ yr}$.

Figs. 2(a) and (b) show the time evolution of the accretion rate \dot{M} and the luminosity L , respectively, along with

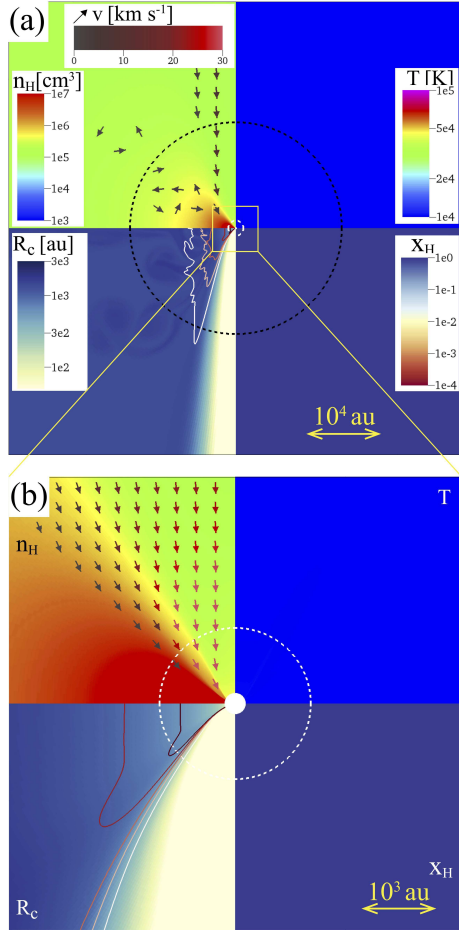


Figure 3. The gas distribution on the scales of (a) 10^4 au and (b) 10^3 au just before turning on the radiation in the fiducial anisotropic radiation run. In each panel, the four quadrants (clockwise from top left) represent number density n_H [cm^{-3}], temperature T [K], neutral fraction of hydrogen x_H and specific angular momentum shown by the corresponding centrifugal radius $R_c (= j^2/GM_{\text{BH}})$ [au]. The arrows represent the velocity vector \mathbf{v} , shown only when $|\mathbf{v}| > 1 \text{ km s}^{-1}$. The contours in the bottom left panel represent $\Omega/\Omega_K = 0.5$ (white), 0.6 (pink), 0.7 (orange), 0.8 (red) and 0.9 (dark red). The Bondi radii for neutral and ionized gases are shown as dashed black and white circles, respectively.

the result for the case with isotropic radiation, which will be described in the next section. Fig. 2(a) shows that during the early period without radiation the accretion rate \dot{M} once converges to the constant value $7.2 \times 10^{-5} M_{\odot} \text{ yr}^{-1}$, only less than 1/10 of the Bondi rate $\dot{M}_B (= 1.7 \times 10^{-3} M_{\odot} \text{ yr}^{-1})$. This remarkable reduction in \dot{M} is totally attributable to the effect of angular momentum.

Fig. 3 shows the gas distribution just before turning on the radiation. A flared disc formed inside r_B can be seen. In the disc, the gravity is balanced with the centrifugal force inside $R_{c,\infty}$ and with the pressure gradient outside $R_{c,\infty}$, so that the dynamical equilibrium ($v_r = v_{\theta} = 0$) is approximately maintained throughout. In the bipolar regions, a gas with low angular momentum directly flows into the sink without hitting on the disc.

Before turning on the radiation, the gas is almost isothermal at $\sim 10^4$ K due to the efficient Ly α cooling

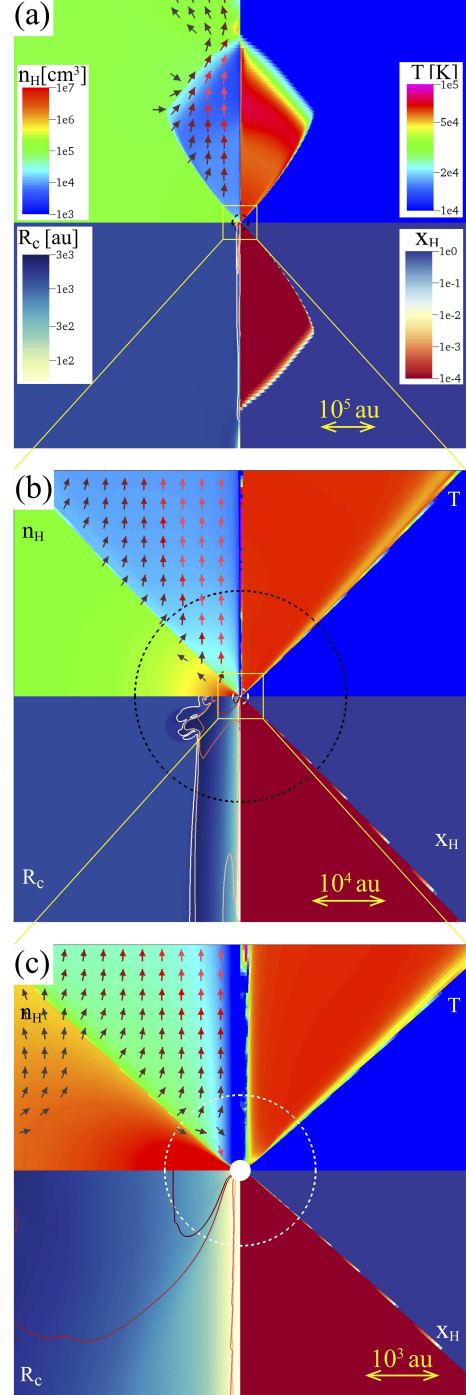


Figure 4. Same as Fig. 3 but at the end of the simulation, when the gas in the polar regions are photoionized by the anisotropic radiation. Here, the gas distribution is plotted on the scales of (a) 10^5 au, (b) 10^4 au and (c) 10^3 au.

throughout the computational domain (see Fig. 3). As an experiment, we have rerun the isothermal simulation setting $T = 10^4$ K and have confirmed that the result does not change. Therefore, in the rest of this paper, we adopt the isothermal equation of state with $T = 10^4$ K in cases without radiation, to save computational costs.

After turning on the radiation, the accretion rate decreases further, as seen in Fig. 2(a). It reaches the smaller

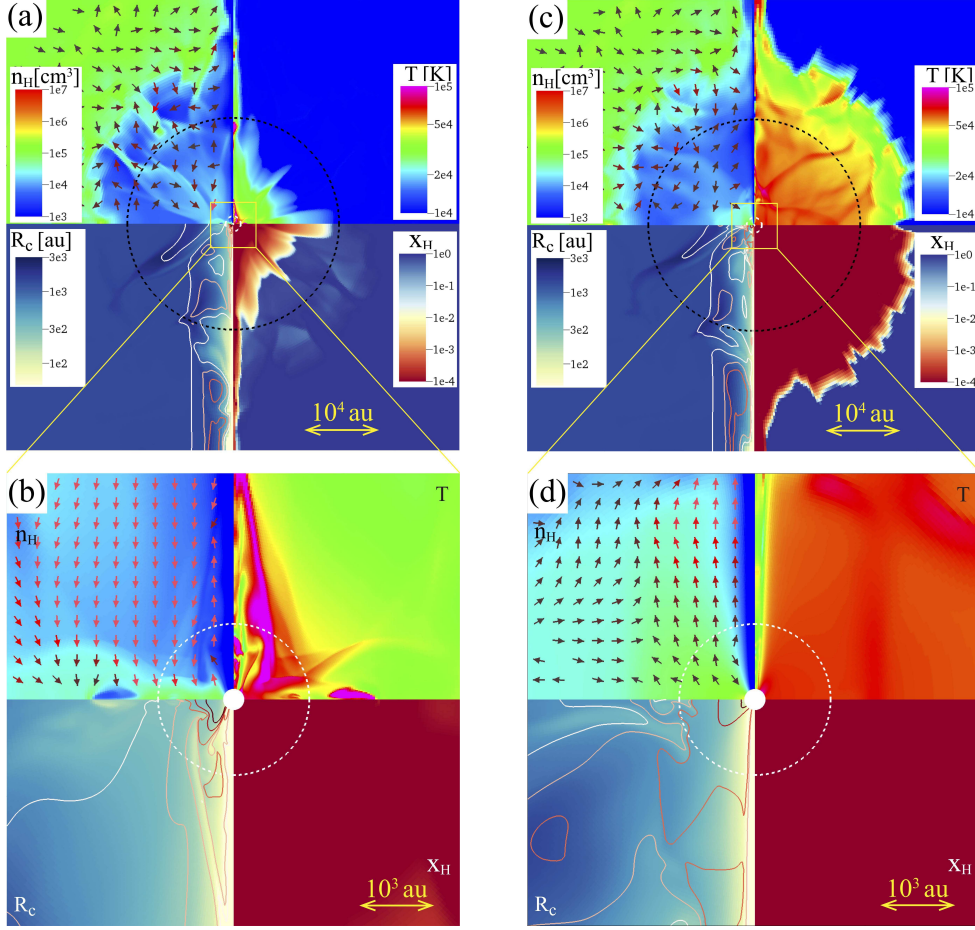


Figure 5. Same as Fig. 3 but (a, b) before and (c, d) after an accretion burst in the isotropic radiation run.

constant value $\dot{M} = 5.0 \times 10^{-6} M_{\odot} \text{yr}^{-1}$ at $t_{\text{end}} = 1.2 \times 10^6$ yr, which is about 0.1 of the value before turning on the radiation and even less than 0.01 of the Bondi rate. As shown in Sugimura et al. (2017), the accretion rate with this parameter set but without rotation is very high with $\dot{M} \sim 0.6 \dot{M}_{\text{B}}$. Therefore, this result demonstrates that the accretion rate is largely reduced by the interplay of angular momentum and radiation. The amount of the reduction will be analytically understood in Sec. 4. In Fig. 2(b), we see that the luminosity behaves in the same way as \dot{M} following Eq. (2). The luminosity L is generally sub-Eddington, with $L \approx 0.2 L_{\text{E}}$ at t_{end} .

Fig. 4 shows the flow structure at t_{end} . The accretion occurs through the neutral disc remaining inside the shadow. The boundary between the ionized and neutral regions is determined by the shadow angle, $\sim 45^\circ$ from the equatorial plane. Outside the Bondi radius for the ionized gas, $r_{\text{B,HII}}$, material on the surface of the neutral gas is photoevaporated and flows out in the vertical direction, as the sound speed, $c_{\text{s,HII}}$, is larger than the escape velocity, $v_{\text{esc}} = (2GM_{\text{BH}}/r)^{1/2}$. Conversely, inside $r_{\text{B,HII}}$, where $c_{\text{s,HII}} < v_{\text{esc}}$, the photoionized gas falls back to the disc again. The outflows in the polar directions blow away the low- j gases initially locating near the poles. Recall that accretion of such material boosted \dot{M} before the radiation is turned on.

In Fig. 4(c), a low-density region appears near the poles as a result of the centrifugal barrier.³ However, structures along the z -axis are partly artifacts of assumed axisymmetry (e.g., Sugimura et al. 2017). In addition, jets or outflows launched near the BH, if included, would largely change such features. Since these structures hardly affect \dot{M} anyway because of the small solid angle, we do not attempt to study them in more detail below.

Although the ionization boundary looks similar in shape to that in the non-rotating case, the flow structure is significantly altered by the angular momentum. Whereas the gas in the shadowed region falls freely in the non-rotating case, it has to pass through the accretion disc slowly in a viscous timescale otherwise. In the non-rotating case with large M_{BH} , Takeo et al. (2018) found that, for a massive enough ($\sim 10^5 M_{\odot}$) BH surrounded by a non-rotating medium, the radiation is obscured by the gas which is pushed by the ram pressure and intrudes into the polar regions, thereby mitigating the radiation feedback. In the rotating case, however, the ram pressure of the flow is so weak that we do not see such a phenomenon. We have confirmed this by performing an additional simulation with M_{BH} enhanced to $10^5 M_{\odot}$.

³ The temperature is also low due to the inefficient photoionization heating, whose heating rate is proportional to the recombination rate and hence the square of the density.

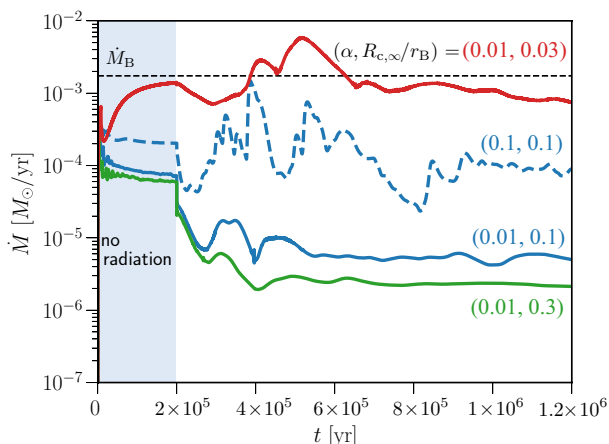


Figure 6. Same as Fig. 2(a) but for the anisotropic radiation runs with different parameter sets. The colours represent $R_{c,\infty}/r_B = 0.03$ (red), 0.1 (blue) and 0.3 (green), while the line types represent $\alpha = 0.01$ (solid) and 0.1 (dashed). The run with $(\alpha, R_{c,\infty}/r_B) = (0.01, 0.1)$ is also presented in Fig. 2(a).

3.2 Isotropic radiation run

Next, we describe the isotropic radiation run. The set-up is the same as in the previous run, except that the radiation is isotropic.

Figs. 2(a) and (b) show the time evolution of \dot{M} and L , respectively. Fig. 2(a) shows that after the radiation is turned on, \dot{M} oscillates violently repeating burst and quiescent phases. This behaviour is similar to what is found in the non-rotating case (e.g., Sugimura et al. 2017), but the averaged accretion rate in the last 10^5 years, $\dot{M} = 1.9 \times 10^{-7} M_\odot \text{ yr}^{-1}$, is about 10 times smaller. Here, we see again the reduction of \dot{M} by the interplay of angular momentum and radiation. Again, Fig. 2(b) shows that L oscillates in the same way as \dot{M} following Eq. (2). Its absolute value is generally small and $L \ll L_E$ even at the burst phases.

Figs. 5 (a, b) and (c, d) show the gas distribution before and after an accretion burst, respectively. The H II region contracts in a quiescent phase, and expands in a burst phase (e.g., Park & Ricotti 2011). The neutral disc initially formed (Fig. 3) is completely ionized and vanishes soon after the radiation is turned on. The H II region is elongated along the z -axis (Figs. 5a and c), because the density decreases near the axis.

3.3 Cases with different sets of the parameters

As described in Sec. 2.3, we also study a number of cases with different parameters of $(\alpha, R_{c,\infty}/r_B) = (0.01, 0.03)$, $(0.1, 0.1)$ and $(0.01, 0.3)$, in addition to the fiducial case presented above. We here only study the evolution of the accretion rates for these cases. More detailed analyses are provided later in Sec. 4, where we develop an analytical model that well explains the numerical results for a wide range of the parameters.

Fig. 6 shows the time variation of \dot{M} in the anisotropic radiation runs with the various parameter sets (see Table 1). By the time radiation turns on ($t \leq 2 \times 10^5 \text{ yr}$), the accretion flows reach steady states. At that time, \dot{M} is larger with larger α , while it is larger with smaller $R_{c,\infty}$ with weak de-

pendence for $R_{c,\infty}/r_B \gtrsim 0.1$. After the radiation turns on, the flows reach different steady states by the end of simulations ($t = 1.2 \times 10^6 \text{ yr}$). The final accretion rates depend on α and $R_{c,\infty}$ in a similar way, but with the greater variation in this case.

In the isotropic radiation runs, \dot{M} oscillates violently as shown in Sec. 3.2, with the average accretion rates for $3 \times 10^5 \text{ yr} < t < 4 \times 10^5 \text{ yr}$ given in Table 1. They are very small in all three runs, with the dependence on α and $R_{c,\infty}$ similar to those obtained above. In this case, the dependence is as weak as before radiation turns on.

4 ANALYTICAL FORMULATION

In the previous section, we found that the angular momentum can largely suppress the accretion in the case with anisotropic radiation, where the accretion rate would be high without angular momentum. In order to understand such suppression, we here develop an analytical model describing accretion through a neutral disc connected to a medium. This model is motivated by the fact that the accretion occurs through the neutral disc remaining inside the shadow in the anisotropic radiation runs (Fig. 4). Note that this model is applicable to neither the case with isotropic radiation where the disc is completely photoionized (Fig. 5), nor that without radiation where polar inflows of low angular momentum gas contribute to the accretion (Fig. 3). In the latter case, however, such polar inflows might be prevented by jets or outflows launched near the BH.

After developing the model, we derive the critical angular momentum of the medium needed to suppress the accretion, as the model predicts that the accretion rate goes back to the Bondi rate in the case with low angular momentum. Using the critical value, we can roughly estimate the impact of the angular momentum on the accretion rate from the property of the medium (e.g., Sec. 5.1).

Below, we first develop the analytical model in Sec. 4.1. Then, in Sec. 4.2, we interpret the simulation results obtained in Sec. 3 with the model. Furthermore, we derive the condition for accretion suppression in Sec. 4.3.

4.1 Analytical model of accretion through a disc connected to a medium

Here, to understand the mechanism of the suppression of accretion by the angular momentum, as well as to analytically estimate the extent of the suppression, we develop an analytical model for the accretion through a neutral disc connected to a rotating medium with constant specific angular momentum $j = j_\infty$. In this model, we suppose that the accretion is suppressed because the gas stagnates at the centrifugal radius and accumulates between the centrifugal and the Bondi radii, and thus the pressure within the Bondi radius is enhanced.

We develop the model by connecting the following two types of solutions at the centrifugal radius $R_{c,\infty}$. Outside $R_{c,\infty}$, where the dynamical equilibrium is held between the gravity, pressure gradient and centrifugal force, the accretion is associated with the inward gas supply that compensates the depletion to the inner disc at $R_{c,\infty}$. Inside $R_{c,\infty}$, where the Keplerian disc is formed, the accretion is caused by the

viscous angular momentum loss, which transports the inward mass flux supplied at $R_{c,\infty}$. Below, we assume that the gas is isothermal.

We start by obtaining the surface density Σ for the outer dynamically equilibrium distribution that is connected to the medium with $\rho = \rho_\infty$ (Papaloizou & Pringle 1984). Here, we assume that the gas has $j = j_\infty$ everywhere. Then, the equation for the force balance can be analytically solved, as shown in Appendix A1. Inside r_B , where the scale height $H_s = c_s/\Omega_K$ is smaller than the radius R and the distribution is disc-like, Σ is given by (Appendix A1)

$$\Sigma = \frac{\sqrt{2\pi}c_s}{\Omega_K}\rho_\infty \exp\left[\frac{r_B}{R} - \frac{R_{c,\infty}r_B}{2R^2}\right]. \quad (9)$$

Next, we obtain the relation between the accretion rate \dot{M} and Σ for the inner viscous Keplerian disc (e.g., Shakura & Sunyaev 1973; Kato et al. 1998; Frank et al. 2002). In Appendix A2, assuming that the disc is thin and adopting the α -type viscosity, $\nu = \alpha \gamma c_s^2/\Omega_K$, we obtain (e.g., Eq. 5.19 of Frank et al. 2002)

$$\dot{M} = 3\pi\nu\Sigma. \quad (10)$$

In a steady accretion disc \dot{M} becomes radially constant by adjusting Σ .

We then connect the two solutions at $R_{c,\infty}$ by substituting Eq. (9) into Eq. (10). We obtain

$$\dot{M}_{\text{suppr}} = \frac{\sqrt{18\pi^3}\alpha\gamma c_s R_{c,\infty}^3}{r_B}\rho_\infty \exp\left[\frac{r_B}{2R_{c,\infty}}\right], \quad (11)$$

where we have used $\Omega_K^2 = c_s^2 r_B/R_{c,\infty}^3$ at $R_{c,\infty}$. Here, if $R_{c,\infty}$ is so small that Eq. (11) yields $\dot{M}_{\text{suppr}} > \dot{M}_B$, the assumption of the outer dynamically-equilibrium distribution breaks down, because the gas cannot be supplied to the disc at a rate exceeding \dot{M}_B . Thus, imposing that \dot{M} does not exceed \dot{M}_B , we modify Eq. (11) as

$$\dot{M} = \begin{cases} \dot{M}_{\text{suppr}} & (\dot{M}_{\text{suppr}} < \dot{M}_B) \\ \dot{M}_B & (\dot{M}_{\text{suppr}} > \dot{M}_B) \end{cases}, \quad (12)$$

which gives an analytical estimate for the accretion rate from a rotating medium.

In Fig. 7, the parameter dependence of the analytical accretion rate \dot{M} is shown, along with the numerical results obtained in the equivalent settings (see Appendix B). In the figure, we normalize \dot{M} by \dot{M}_B . Note that how much \dot{M} is suppressed with respect to \dot{M}_B depends only on the combination of α and $R_{c,\infty}/r_B$ (not on either M_{BH} , ρ_∞ or c_s), because, with Eqs. (1) and (11), $\dot{M}_{\text{suppr}}/\dot{M}_B$ can be rewritten as

$$\frac{\dot{M}_{\text{suppr}}}{\dot{M}_B} = 2.8\alpha \left(\frac{R_{c,\infty}}{r_B}\right)^3 \exp\left[\frac{r_B}{2R_{c,\infty}}\right], \quad (13)$$

where we have used $\gamma = 5/3$. The agreement of the analytical and numerical results is remarkable considering the simplicity of the model. In the case that the accretion is suppressed by the angular momentum, i.e., $\dot{M}_{\text{suppr}} < \dot{M}_B$, the α dependence is that \dot{M} is proportional to α (Eq. 11). As for the $R_{c,\infty}$ dependence, \dot{M} rapidly increases with decreasing $R_{c,\infty}$ for $R_{c,\infty} \lesssim 0.1 r_B$, mainly because of the exponential increase of $\Sigma(R_{c,\infty})$ under the assumption of the dynamical equilibrium (see Eq. 9). When \dot{M}_{suppr} reaches \dot{M}_B , however, the dynamical equilibrium is broken and the increase of \dot{M}

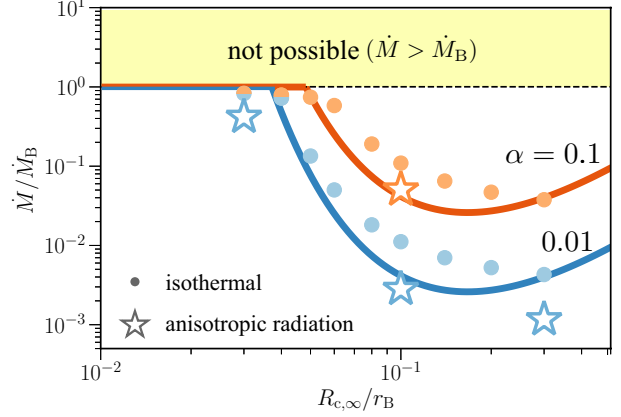


Figure 7. The parameter dependence of \dot{M} for the accretion from an isothermal medium with $j = j_\infty$. We normalize \dot{M} by \dot{M}_B . The horizontal axis represents $R_{c,\infty}$ ($\equiv j_\infty^2/GM_{\text{BH}}$), while the colors correspond to $\alpha = 0.1$ (orange) and 0.01 (blue). The lines are the analytical estimates given by Eq. (12), whereas the filled dots are the numerical values obtained in Appendix B. We overplot the results of anisotropic radiation runs in Sec. 3 with open stars.

stops. For lower $R_{c,\infty}$, \dot{M} is equal to \dot{M}_B , with little effect of the angular momentum. The disagreement between the numerical and analytical results can be partly attributed to the considerable thickness of disc at $R_{c,\infty}$ (see Fig. B1c), which is not consistent with our assumption of thin inner disc. As the thickness at $R_{c,\infty}$ increases with $R_{c,\infty}$ and the aspect ratio reaches unity when $R_{c,\infty} \sim r_B$, our model is reliable only when $R_{c,\infty}$ is sufficiently smaller than r_B .

4.2 Interpreting the simulation results with the analytical model

In this section, we understand the simulation results in Sec. 3 with the analytical model developed in the previous section, focusing mainly on the case with anisotropic radiation. We begin with overplotting the simulation results (star symbols) in Fig. 7, where the parameter dependence of \dot{M} in the model (lines), as well as that for the isothermal accretion (dot symbols), is shown. For all the four cases with $(\alpha, R_{c,\infty}/r_B) = (0.01, 0.1)$, $(0.1, 0.01)$, $(0.01, 0.03)$ and $(0.01, 0.3)$ examined in this paper, the simulation results are well reproduced by the model. Especially, the transition between low and high- \dot{M} regimes occurring at $R_{c,\infty}/r_B \lesssim 0.1$ is clearly seen both in the simulation results and the model. The accretion rate in the run with $(\alpha, R_{c,\infty}/r_B) = (0.01, 0.03)$ is $\sim 0.5 \dot{M}_B$, which is close to the value obtained with the assumption of negligible angular momentum in the run with the same anisotropic radiation field (Sugimura et al. 2017). The downward shifts of \dot{M} by at most a factor of three compared to the isothermal case (dot symbols) are partly attributable to the photoevaporation mass-loss from the surface of the disc. Note that we have also confirmed that the equatorial gas profile in the anisotropic radiation run with $\alpha = 0.01$ and $R_{c,\infty} = 0.1 r_B$ is consistent with that of the model (Appendix C). The agreement both in the accretion rate and the gas profile suggests that the accretion is suppressed by the same mechanism as in the model, i.e., it is due to the stagnation of the gas at the centrifugal radius

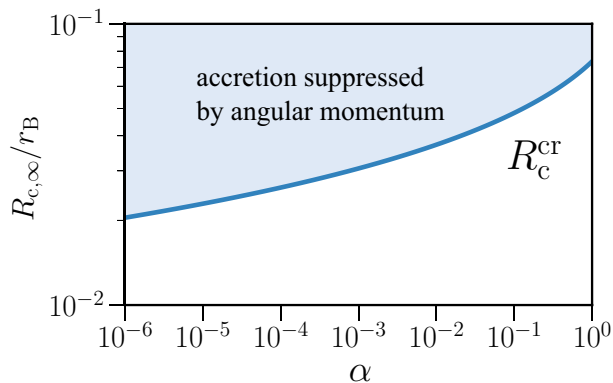


Figure 8. The critical centrifugal radius R_c^{cr} normalized by r_B as a function of α . The accretion is significantly suppressed by the angular momentum in the shaded region ($R_{c,\infty} > R_c^{\text{cr}}$).

and the consequent pressure enhancement within the Bondi radius.

Below, we make some remarks on the simulation results in the case without radiation, as well as in the case with isotropic radiation (see Table 1). In the former case, the accretion rates for the runs with $(\alpha, R_{c,\infty}/r_B) = (0.01, 0.1)$, $(0.1, 0.1)$ and $(0.01, 0.3)$ are larger than in the model, because, in addition to the accretion through the disc, the polar low- j gas directly flows into the sink and contributes to the accretion rate (see Fig. 3). Recall that in the anisotropic radiation runs, polar photoevaporative outflows prevent such inflows. For the run with $(\alpha, R_{c,\infty}/r_B) = (0.01, 0.03)$, however, \dot{M} at $t = 2 \times 10^5$ yr is $0.8 \dot{M}_B$ and slightly lower than \dot{M}_B as predicted by the model, because at that point of time \dot{M} has yet to reach the asymptotic value and is still on the rise. Conversely, in the latter case, the accretion rates are smaller than in the model, because the accretion disc is totally photoevaporated (see Fig. 5). In the anisotropic radiation runs, however, the disc survives without being photoevaporated inside the shadow.

4.3 Condition for accretion suppression by the angular momentum

Next, we obtain the critical angular momentum above which the accretion is significantly suppressed.

As mentioned in Sec. 4.1, we suppose that the effect of angular momentum becomes negligible when Eq. (13) yields $\dot{M}_{\text{suppr}}/\dot{M}_B > 1$. Thus, we define the critical centrifugal radius R_c^{cr} by the condition $\dot{M}_{\text{suppr}}/\dot{M}_B = 1$. In Fig. 8, we plot R_c^{cr} as a function of α . The former slowly increases with the latter, with $R_c^{\text{cr}} = 0.04 r_B$ at $\alpha = 0.01$ ($R_c^{\text{cr}} = 0.05 r_B$ at $\alpha = 0.1$). For a wide range of α with $10^{-6} < \alpha < 1$, the suppression of accretion becomes important as $R_{c,\infty}$ exceeds $O(10^{-2} r_B)$, with \dot{M} decreased to $O(\alpha \dot{M}_B)$ when $R_{c,\infty} \sim 10^{-1} r_B$ (see Fig. 7). Recall that the case with $R_{c,\infty} \gtrsim r_B$ is beyond the scope of our analytical model (Sec. 4.1).

As expected with our analyses in Sec. 4.2, Fig. 8 agrees well with the numerical results overall. Most of the anisotropic radiation runs examined are located in the shaded region, showing the significant suppression of the ac-

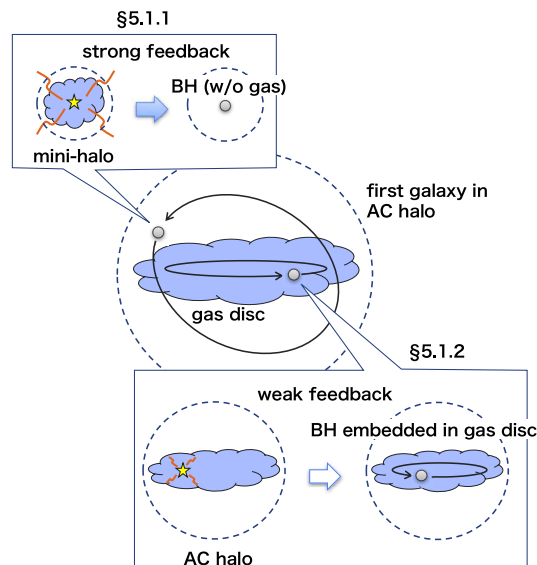


Figure 9. Two evolutionary paths of a Pop III remnant BH and its environment. A Pop III remnant BH can form either in a mini-halo (Sec. 5.1.1) or in an atomic-cooling (AC) halo (Sec. 5.1.2). See text for details.

cretion rate. Only an exception is the case with $(R_{c,\infty}, \alpha) = (0.03, 0.01)$, which is really below the critical line in Fig. 8.

5 DISCUSSION

5.1 Growth of Pop III remnant BHs

Rapid growth of BHs is critically important for the formation of SMBHs in the early Universe, especially if their growth starts from “light seeds”, i.e., the Pop III remnant BHs. Reflecting the expected diversity of the stellar mass of the Pop III stars (e.g., Hirano et al. 2014, 2015), their remnant BHs would have a variety of masses, $\sim 100 - 10^3 M_\odot$. The subsequent growth of such BHs should depend on the environments surrounding them (Fig. 9). In the standard bottom-up structure formation paradigm in the Λ CDM Universe, Pop III stars normally form in mini-halos with masses of $M_h \simeq 10^{5-6} M_\odot$ at $z > 20$ (e.g. Yoshida et al. 2006). In addition, Pop III stars also form in atomic-cooling halos with $M_h \gtrsim 3 \times 10^7 M_\odot$, if prior star formation is hampered by Lyman-Werner radiation and/or baryonic streaming motions (e.g., Wise & Abel 2007b; Visbal et al. 2014; Tanaka & Li 2014; Hirano et al. 2017; Schauer et al. 2017). In the following, we discuss the possibility of rapid growth of Pop III remnant BHs, separately considering their different formation sites of mini-halos and atomic-cooling halos. We argue that the BH growth via rapid mass accretion is not easily realized for either case. In particular, the angular momentum effect studied in the previous sections is a critical obstacle for the growth of BHs formed in atomic-cooling halos.

5.1.1 Pop III remnants formed in mini-halos

Let us first consider the growth of Pop III remnant BHs in a mini-halo with $M_h \simeq 10^{5-6} M_\odot$. Massive Pop III stars with $\gtrsim 10^2 - 10^3 M_\odot$ produce intense ionizing radiation

before collapsing into BHs. This ionizing radiation feedback evacuates a large fraction of gas from the mini-halo, because of its shallow gravitational potential (Kitayama et al. 2004). Rapid mass accretion on to the remnant BH is thus not expected, at least when the BH is still harbored in the same mini-halo (Johnson & Bromm 2007).

Through the assembly of DM halos, a significant fraction of Pop III remnant BHs fall into an atomic-cooling halo with $M_h \gtrsim 3 \times 10^7 M_\odot$ at $z \lesssim 15$. In such a massive and gas-rich halo, the BHs could grow via accretion if they could sink to the galactic disc due to dynamical friction. We assume that a fraction f_* ($\simeq 0.3$) of the gas in the halo forms stars, i.e., $M_* = f_*(\Omega_b/\Omega_m)M_h$, and those stars exert friction on the remnant BHs. Here, we adopt $\Omega_b/\Omega_m = 0.16$ (Planck Collaboration et al. 2016). If the density distribution of the stars is approximated by a singular isothermal sphere, the dynamical friction timescale for a BH⁴ is estimated as (Binney & Tremaine 1987)

$$t_{\text{DF}} \simeq \frac{1.17}{\ln \Lambda} \frac{M_*}{M_{\text{BH}}} t_{\text{cross}},$$

$$\simeq 0.7 \text{ Gyr } M_{\text{h},7.5}^{1/2} M_{\text{BH},3}^{-1} \left(\frac{f_*}{0.3}\right)^{1/2} \left(\frac{r}{50 \text{ pc}}\right)^{3/2}, \quad (14)$$

where the crossing time is $t_{\text{cross}} = \sqrt{r^3/(GM_*)}$ and the Coulomb logarithm is set to $\ln \Lambda \sim \ln[M_*/M_{\text{BH}}] \sim 6$. In the above expression, we have defined $M_{\text{h},7.5} \equiv M_h/3 \times 10^7 M_\odot$ and $M_{\text{BH},3} \equiv M_{\text{BH}}/10^3 M_\odot$. We assume that the BH is located at the outskirts of the galactic disc, i.e., $r \simeq \lambda R_{\text{vir}}$ (Mo et al. 1998), where $\lambda \simeq 0.05$ is the dimensionless spin parameter and $R_{\text{vir}} \simeq 1 \text{ kpc } M_{\text{h},7.5} (1+z)_{16}^{-1}$ is the virial radius of the halo (Barkana & Loeb 2001), with $(1+z)_{16} \equiv (1+z)/16$. Using this relation, the ratio of the dynamical friction timescale to the Hubble timescale is estimated as

$$\frac{t_{\text{DF}}}{t_{\text{H}}} \simeq 2 M_{\text{h},7.5}^2 M_{\text{BH},3}^{-1} \lambda_{0.05}^{3/2} \left(\frac{f_*}{0.3}\right)^{1/2}, \quad (15)$$

with $\lambda_{0.05} = \lambda/0.05$. This suggests that dynamical friction is inefficient for BHs with $M_{\text{BH}} \lesssim 10^3 M_\odot$. As a result, Pop III remnant BHs coming originally from mini-halos will just continue to wander in the outskirts of the galactic disc. Such BHs will hardly grow via accretion, simply because the density of the surrounding gas is low ($n_{\text{H}} \ll 10^4 \text{ cm}^{-3}$, also see §5.1.2 below). In this case, the rapid growth of BHs is unlikely to occur regardless of whether the angular momentum of the gas affects the BH feeding.

5.1.2 Pop III remnants formed in atomic-cooling halos

Pop III stars can be also formed in a galactic disc in an atomic-cooling halo with $M_h \gtrsim 3 \times 10^7 M_\odot$ (or $T_{\text{vir}} \gtrsim 10^4 \text{ K}$). Such a halo can hold the gas against the stellar feedback (Kitayama et al. 2004). The remnant BHs are initially embedded in the gas-rich disc.

Let us suppose that the BH is embedded in an isothermal, exponential disc with a gas temperature $T_{\text{gas}} \simeq 8000 \text{ K}$.

⁴ Note that the dynamical friction timescale could be shortened by a factor of two if the friction is exerted by a gas instead of stars (Ostriker 1999; Escala et al. 2004)

The gas density at the mid-plane within the disc radius ($r \lesssim \lambda R_{\text{vir}}$) is estimated as (Oh & Haiman 2002)

$$n_{\text{H}} \simeq 1 \times 10^4 \text{ cm}^{-3} T_{\text{vir},4} \lambda_{0.05}^{-4} (1+z)_{16}^3 \left(\frac{f_{\text{d}}}{0.3}\right)^2. \quad (16)$$

Assuming that a remnant BH has a peculiar velocity comparable to the circular velocity of the gas disc,

$$V = \sqrt{\frac{G(M_{\text{d}} + M_*)}{\lambda R_{\text{vir}}}}$$

$$\simeq 20 \text{ km s}^{-1} T_{\text{vir},4}^{1/2} \lambda_{0.05}^{-1/2} \left(\frac{f_{\text{d}} + f_*}{0.6}\right)^{1/2}, \quad (17)$$

which is higher than the sound speed of the gas $c_s \simeq 7 \text{ km s}^{-1} (T_{\text{gas}}/8000 \text{ K})^{1/2}$. Thus, the Bondi-Hoyle-Lyttleton (BHL) accretion rate is reduced by a factor of $\simeq [1 + (V/c_s)^2]^{3/2} \simeq 20$ from the value in Eq. (1),

$$\dot{M}_{\text{BHL}} \simeq 1 \times 10^{-5} M_\odot \text{ yr}^{-1} \left(\frac{f_{\text{d}}}{0.3}\right)^{1/2} \left(\frac{f_{\text{d}} + f_*}{2f_{\text{d}}}\right)^{-3/2}$$

$$\times T_{\text{vir},4}^{-1/2} M_{\text{BH},3}^2 \lambda_{0.05}^{-5/2} (1+z)_{16}^3. \quad (18)$$

Note that Eq. (18) is valid for $(V/c_s)^2 \gg 1$. The typical BH growth timescale is $t_{\text{grow}} \sim M_{\text{BH}}/\dot{M}_{\text{BHL}} \sim 100 \text{ Myr } M_{\text{BH},3}^{-1} (1+z)_{16}^{-3}$. Thus, we obtain $t_{\text{grow}}/t_{\text{H}} \sim 0.3 M_{\text{BH},3}^{-1} (1+z)_{16}^{-3/2}$, which means that Pop III remnant BHs with $M_{\text{BH}} \gtrsim 3 \times 10^2 M_\odot$ formed inside an atomic-cooling halo may undergo rapid accretion. *However, the angular momentum of the accreting gas here comes into play to prevent the BH growth.*

According to cosmological simulations of the first galaxy, the gas flow in an atomic-cooling halo is turbulent in general (e.g., Wise & Abel 2007a). We consider the same density fluctuation of the turbulent medium as in our Galaxy, $\delta\rho/\rho \sim (L/2 \text{ pc})^{1/3}$, where L is the characteristic spatial length of the fluctuation (Armstrong et al. 1995; Draine 2011). Accreting gas with such density fluctuation brings a net angular momentum, which is estimated as $\ell \sim (V r_{\text{B}}/4) \cdot (\delta\rho/\rho)|_{L=2r_{\text{B}}}$ (Ipser & Price 1977; Ioka et al. 2017; Matsumoto et al. 2018). Thus, the ratio of the centrifugal radius to the Bondi radius is given by

$$\frac{R_{\text{c}}}{r_{\text{B}}} \simeq 3 \times 10^{-2} M_{\text{BH},3}^{2/3} \left(\frac{V}{20 \text{ km s}^{-1}}\right)^{-4/3}. \quad (19)$$

This ratio is comparable to the critical value $R_{\text{c}}^{\text{cr}}/r_{\text{B}} \sim 0.04$ obtained in Sec. 4.3, above which the accretion rate is suppressed by a factor of $\alpha \sim O(0.01-0.1)$, but the former exceeds the latter as M_{BH} becomes larger than $\sim 10^3 M_\odot$. Thereafter, even if the BH is embedded in the gas disc, its growth timescale becomes even longer than the age of the Universe at $z = 6$,

$$t_{\text{grow}}^{\text{ang}} \sim \frac{M_{\text{BH}}}{M_{\text{suppr}}} \sim 10 \text{ Gyr } M_{\text{BH},3}^{-1} (1+z)_{16}^{-3} \alpha_{-2}, \quad (20)$$

where $\alpha_{-2} \equiv \alpha/10^{-2}$. Therefore, it seems that *Pop III remnant BHs are hard to grow to high- z SMBHs via rapid accretion.*

5.1.3 Possible pathways for rapid growth of Pop III remnant BHs

A number of previous studies (e.g., Volonteri & Rees 2005; Madau et al. 2014; Alexander & Natarajan 2014; Volonteri

et al. 2015; Tagawa et al. 2015; Ryu et al. 2016; Pacucci et al. 2017) have investigated the possibility of rapid (super-Eddington, i.e., $\dot{M} > 10 \dot{M}_E$ and thus $L > L_E$) gas accretion of Pop III remnant BHs to explain the existence of high- z SMBHs. Since our speculation seems different from those works, we discuss what kind of uncertainties lead to the discrepancies, comparing to our arguments in §5.1.1 and 5.1.2.

Tagawa et al. (2015) and Ryu et al. (2016) considered the evolution of Pop III remnant BHs in an atomic-cooling halo, performing N-body simulations. In fact, they concluded that some remnant BHs can fall into the central region much faster than we estimated. This is mainly because the gas density is assumed to be higher than $\sim 10^4 \text{ cm}^{-3}$ or to follow an isothermal singular profile ($n_H \propto r^{-2}$). Because of the higher gas densities (at smaller scales), dynamical friction allows the BHs to quickly sink into the galactic center. When the remnant BH reaches the central region with $n_H \gtrsim 10^6 \text{ cm}^{-3} M_{\text{BH},3}^{-1}$, the Bondi accretion rate on to it becomes high enough ($\sim 5000 L_E/c^2$) to realize hyper-Eddington accretion without impeded by radiation feedback (Inayoshi et al. 2016; Sakurai et al. 2016; Sugimura et al. 2017; Takeo et al. 2018). This process may quickly form intermediate massive BHs with $\sim 10^5 M_\odot$ at the centre of the protogalaxy.

Obviously, a key uncertainty is the density structure of the gas containing the BHs. Tagawa et al. (2015) and Ryu et al. (2016) assume that the density profile does not change during the orbital evolution of BHs. In reality, however, the star formation will easily occur in the high-density regions, so that the original density structure could be modified by feedback effects such as supernova explosions (e.g., Dubois et al. 2015; Yajima et al. 2017). In future work, we will study the evolution of the BH orbital motions and ambient density structure, self-consistently incorporating the feedback effects. Such treatment will also allow us to accurately estimate how much angular momentum is brought by the accreting gas, and to assess whether super-Eddington accretion is possible circumventing the angular momentum barrier presented in this paper.

5.2 Caveats

We have made a number of simplifications and approximations in this work, and now discuss their significances.

First, we have examined only the two limiting cases of the anisotropy of radiation field. In the case of a non-rotating medium, Sugimura et al. (2017) have found that there is a critical shadowing angle ($\sim 10^\circ$ from the equatorial plane) above which the efficient accretion is realized by the neutral Bondi-like inflows through the equatorial layer that exceeds the photoevaporative mass-loss from the surfaces. In the rotating case, however, the above condition needs to be modified, because the photoevaporative mass-loss from the surfaces of the rotationally-supported disc can be significant. We have seen that the disc is completely ionized by the isotropic radiation, while it is not photoevaporated inside the $\sim 45^\circ$ shadow in the case of the anisotropic radiation. We will study the dependence of \dot{M} on the anisotropy more in the future.

Second, the actual anisotropy created inside the sink is highly uncertain, although \dot{M} strongly depends on it. In

the literature, generation of (failed) winds or coronae above the disc have been investigated (e.g., Hollenbach et al. 1994; Begelman et al. 1983; Woods et al. 1996; Proga et al. 2000; Wada 2012; Suzuki & Inutsuka 2014; Nomura et al. 2016). We expect that the materials associated with such structures obscure the outward radiation and create its anisotropy. In a future work, we plan to study such process, considering its dependence on M_{BH} , \dot{M} , the metallicity of gas, etc..

Third, we have studied the idealized system of a static BH embedded in a homogeneous medium, in order to understand how angular momentum and radiation feedback affect the accretion flow. In considering more realistic BH accretion systems, however, we need to take into account the effects of turbulence (e.g., Krumholz et al. 2006; Hobbs et al. 2011) and/or galactic-scale inflows (e.g., Hobbs et al. 2012; Park et al. 2016). In a highly symmetric system as studied by our axisymmetric 2D simulations, the angular momentum transported outward through a disc may accumulate near the disc outer edge, resulting in the reduction of the accretion rate. We in fact confirm this effect for the cases where the accreting gas has small angular momentum ($R_{c,\infty} \ll 0.1 r_B$; see Appendix B). In the case of accretion from a turbulent medium, however, such accumulation may not occur because the disc can change its rotational axis before the accumulation proceeds, as the angular momentum vector of the accreting gas varies in time. Recall that in this work, we have artificially removed the accumulated angular momentum by imposing upper bound on specific angular momentum. This procedure may qualitatively mimic the above mechanism that works in a turbulent medium.

Fourth, we have adopted the α -type viscosity to mimic the angular momentum transport via the turbulence driven by the MRI. Although our results depend on the value of α , as well as where the viscosity works, i.e., the confinement factor f in Eq. (8), it is computationally too expensive to perform 3D magnetohydrodynamics simulations of the same problem. The unstable non-axisymmetric modes can also affect the flow in the 3D simulations (Papaloizou & Pringle 1984). In the cases studied here, the Toomre Q parameter is above unity and the disc is gravitationally stable. In a case with different parameter set, however, the gravitational instability can play a role in transporting the angular momentum depending on M_{BH} and $n_{\text{H},\infty}$ (see Appendix E). It is also likely that the Rayleigh-Taylor instability of the HII bubble, as seen in our 2D simulations (e.g., Fig. 5), grows differently in 3D. The former 3D simulations (Park et al. 2017), however, suggest that such difference does not significantly change the accretion rate. In addition, the disc is known to be Rayleigh-unstable when the angular momentum decreases outward, so that the accumulated angular momentum would be transported in 3D simulations (see, e.g., Inayoshi et al. 2018, and reference therein).

Finally, although we assume that the dominant cooling process in the neutral gas is the Ly α cooling, the H $^-$ free-bound cooling becomes dominant and cools the gas to $\sim 4 \times 10^3 \text{ K}$ when $n_{\text{H}} \gg 10^6 \text{ cm}^{-3}$ (Omukai 2001). In addition, the temperature might drop even to $\sim 2 \times 10^2 \text{ K}$ if H $_2$ molecules somehow form in spite of the UV irradiation from the BH neighbourhood. Consideration of these processes could lead to modification of \dot{M} .

6 SUMMARY

We have investigated the combined effect of gas angular momentum and radiation feedback on seed BH accretion, by performing a suit of 2D axisymmetric simulations considering both finite gas angular momentum and radiation from the circum-BH disc. The BH is located at the center of a rotating medium, whose centrifugal radius is typically a tenth of the Bondi radius. We follow the formation of the rotationally-supported disc, through which the accretion proceeds by the angular momentum transport due to the assumed α -type viscosity.

We have found that the accretion is strongly suppressed by the gas angular momentum. Except for the case with very low angular momentum, the accretion rate is reduced by one order of magnitude even without radiation feedback and becomes even smaller with the feedback. In particular, the accretion rate in the case with anisotropic radiation field, which would be in the same order as the Bondi rate without gas rotation (Sugimura et al. 2017), is reduced by a factor of $\alpha \sim O(0.01 - 0.1)$. Our results clearly indicate the importance of the interplay of the angular momentum and radiation feedback.

We have also developed an analytical model that describes accretion through a neutral disc connected to a medium. This model is capable of reproducing the accretion rate obtained in the simulations with anisotropic radiation. Furthermore, the model suggests the presence of the critical angular momentum above which the accretion is significantly suppressed. The corresponding critical centrifugal radius normalized by the Bondi radius is a weakly increasing function of α and equal to 0.04 for $\alpha = 0.01$, suggesting that even such small angular momentum is enough to reduce the accretion rate. This provides a useful estimate for the impact of the angular momentum on the accretion rate, for example, in future cosmological simulations of SMBH formation.

Finally, we have discussed the implications of our findings on the growth of Pop III remnant BHs. In the literature, those BHs are claimed to grow to high- z SMBHs by very rapid (super-Eddington) accretion. However, the angular momentum effect studied in this paper can be a crucial obstacle for such rapid mass accretion. Whilst the condition for the formation of direct-collapse BHs is known to be difficult to achieve (e.g., Sugimura et al. 2014), it should be equally challenging for the Pop III remnant BHs to rapidly grow via the super-Eddington accretion. Clearly, further studies are needed to unveil the nature.

ACKNOWLEDGEMENTS

The authors would like to thank Ken Ohsuga, Sanemichi Takahashi and Kenji Toma for fruitful discussions. The numerical simulations were performed on the Cray XC30 at CfCA of the National Astronomical Observatory of Japan, as well as on the computer cluster, *Draco*, at Frontier Research Institute for Interdisciplinary Sciences of Tohoku University and on the Cray XC40 at Yukawa Institute for Theoretical Physics in Kyoto University. This work is supported in part by MEXT/JSPS KAKENHI Grant Number 15J03873 (KS), 25800102, 15H00776 and 16H05996 (TH),

17H04827 (HY) and 17H01102 and 17H06360 (KO) and by the Simons Foundation through the Simons Society of Fellows (KI).

REFERENCES

- Abramowicz, M. A., Czerny, B., Lasota, J. P., & Szuszkiewicz, E. 1988, *ApJ*, 332, 646
- Alexander, T., & Natarajan, P. 2014, *Science*, 345, 1330
- Armstrong, J. W., Rickett, B. J., & Spangler, S. R. 1995, *ApJ*, 443, 209
- Bai, X.-N., & Stone, J. M. 2013, *ApJ*, 767, 30
- Balbus, S. A., & Hawley, J. F. 1998, *Reviews of Modern Physics*, 70, 1
- Barai, P., Proga, D., & Nagamine, K. 2012, *MNRAS*, 424, 728
- Barkana, R., & Loeb, A. 2001, *Phys. Rep.*, 349, 125
- Begelman, M. C., McKee, C. F., & Shields, G. A. 1983, *ApJ*, 271, 70
- Begelman, M. C., & Volonteri, M. 2017, *MNRAS*, 464, 1102
- Binney, J., & Tremaine, S. 1987, *Galactic dynamics*
- Bondi, H. 1952, *MNRAS*, 112, 195
- Bromm, V., & Loeb, A. 2003, *ApJ*, 596, 34
- Chon, S., Hirano, S., Hosokawa, T., & Yoshida, N. 2016, *ApJ*, 832, 134
- Ciotti, L., & Ostriker, J. P. 2001, *ApJ*, 551, 131
- Cuadra, J., Nayakshin, S., Springel, V., & Di Matteo, T. 2006, *MNRAS*, 366, 358
- Devecchi, B., & Volonteri, M. 2009, *ApJ*, 694, 302
- Draine, B. T. 2011, *Physics of the Interstellar and Inter-galactic Medium* (Princeton University Press)
- Dubois, Y., Volonteri, M., Silk, J., et al. 2015, *MNRAS*, 452, 1502
- Escala, A., Larson, R. B., Coppi, P. S., & Mardones, D. 2004, *ApJ*, 607, 765
- Fan, X., Narayanan, V. K., Lupton, R. H., et al. 2001, *AJ*, 122, 2833
- Frank, J., King, A., & Raine, D. J. 2002, *Accretion Power in Astrophysics: Third Edition*, 398
- Gallerani, S., Fan, X., Maiolino, R., & Pacucci, F. 2017, *PASA*, 34, e022
- Gaspari, M., Brighenti, F., & Temi, P. 2015, *A&A*, 579, A62
- Haiman, Z. 2013, in *Astrophysics and Space Science Library*, Vol. 396, *The First Galaxies*, ed. T. Wiklind, B. Mobasher, & V. Bromm, 293
- Hirano, S., Hosokawa, T., Yoshida, N., & Kuiper, R. 2017, *Science*, 357, 1375
- Hirano, S., Hosokawa, T., Yoshida, N., Omukai, K., & Yorke, H. W. 2015, *MNRAS*, 448, 568
- Hirano, S., Hosokawa, T., Yoshida, N., et al. 2014, *ApJ*, 781, 60
- Hobbs, A., Nayakshin, S., Power, C., & King, A. 2011, *MNRAS*, 413, 2633
- Hobbs, A., Power, C., Nayakshin, S., & King, A. R. 2012, *MNRAS*, 421, 3443
- Hollenbach, D., Johnstone, D., Lizano, S., & Shu, F. 1994, *ApJ*, 428, 654
- Hosokawa, T., Hirano, S., Kuiper, R., et al. 2016, *ApJ*, 824, 119

- Hosokawa, T., Omukai, K., & Yorke, H. W. 2012, *ApJ*, 756, 93
- Hosokawa, T., Omukai, K., Yoshida, N., & Yorke, H. W. 2011, *Science*, 334, 1250
- Igumenshchev, I. V., & Abramowicz, M. A. 1999, *MNRAS*, 303, 309
- Inayoshi, K., Haiman, Z., & Ostriker, J. P. 2016, *MNRAS*, 459, 3738
- Inayoshi, K., Omukai, K., & Tasker, E. 2014, *MNRAS*, 445, L109
- Inayoshi, K., Ostriker, J. P., Haiman, Z., & Kuiper, R. 2018, *MNRAS*, arXiv:1709.07452
- Ioka, K., Matsumoto, T., Teraki, Y., Kashiyama, K., & Murase, K. 2017, *MNRAS*, 470, 3332
- Ipsier, J. R., & Price, R. H. 1977, *ApJ*, 216, 578
- Johnson, J. L., & Bromm, V. 2007, *MNRAS*, 374, 1557
- Kato, S., Fukue, J., & Mineshige, S. 1998, *Black-hole accretion disks* (Kyoto University Press)
- Katz, H., Sijacki, D., & Haehnelt, M. G. 2015, *MNRAS*, 451, 2352
- Kawaguchi, T., & Mori, M. 2010, *ApJ*, 724, L183
- Kawakatu, N., & Wada, K. 2008, *ApJ*, 681, 73
- Kitayama, T., Yoshida, N., Susa, H., & Umemura, M. 2004, *ApJ*, 613, 631
- Krumholz, M. R., McKee, C. F., & Klein, R. I. 2006, *ApJ*, 638, 369
- Kuiper, R., Klahr, H., Beuther, H., & Henning, T. 2010a, *ApJ*, 722, 1556
- . 2011, *ApJ*, 732, 20
- Kuiper, R., Klahr, H., Dullemond, C., Kley, W., & Henning, T. 2010b, *A&A*, 511, A81
- Kuiper, R., & Klessen, R. S. 2013, *A&A*, 555, A7
- Kurosawa, R., & Proga, D. 2009, *ApJ*, 693, 1929
- Li, J., Ostriker, J., & Sunyaev, R. 2013, *ApJ*, 767, 105
- Madau, P., Haardt, F., & Dotti, M. 2014, *ApJ*, 784, L38
- Matsumoto, T., Teraki, Y., & Ioka, K. 2018, *MNRAS*, 475, 1251
- Mignone, A., Bodo, G., Massaglia, S., et al. 2007, *ApJS*, 170, 228
- Milosavljević, M., Couch, S. M., & Bromm, V. 2009, *ApJ*, 696, L146
- Mo, H. J., Mao, S., & White, S. D. M. 1998, *MNRAS*, 295, 319
- Mortlock, D. J., Warren, S. J., Venemans, B. P., et al. 2011, *Nature*, 474, 616
- Nomura, M., Ohsuga, K., Takahashi, H. R., Wada, K., & Yoshida, T. 2016, *PASJ*, 68, 16
- Novak, G. S., Ostriker, J. P., & Ciotti, L. 2011, *ApJ*, 737, 26
- Oh, S. P., & Haiman, Z. 2002, *ApJ*, 569, 558
- Omukai, K. 2001, *ApJ*, 546, 635
- Omukai, K., Schneider, R., & Haiman, Z. 2008, *ApJ*, 686, 801
- Ostriker, E. C. 1999, *ApJ*, 513, 252
- Pacucci, F., Natarajan, P., Volonteri, M., Cappelluti, N., & Urry, C. M. 2017, *ApJ*, 850, L42
- Papaloizou, J. C. B., & Pringle, J. E. 1984, *MNRAS*, 208, 721
- Park, K., & Ricotti, M. 2011, *ApJ*, 739, 2
- . 2012, *ApJ*, 747, 9
- Park, K., Ricotti, M., Natarajan, P., Bogdanović, T., & Wise, J. H. 2016, *ApJ*, 818, 184
- Park, K., Wise, J. H., & Bogdanović, T. 2017, *ApJ*, 847, 70
- Planck Collaboration, Ade, P. A. R., Aghanim, N., et al. 2016, *A&A*, 594, A13
- Proga, D., & Begelman, M. C. 2003a, *ApJ*, 582, 69
- . 2003b, *ApJ*, 592, 767
- Proga, D., Stone, J. M., & Kallman, T. R. 2000, *ApJ*, 543, 686
- Ryu, T., Tanaka, T. L., Perna, R., & Haiman, Z. 2016, *MNRAS*, 460, 4122
- Sakurai, Y., Inayoshi, K., & Haiman, Z. 2016, *MNRAS*, 461, 4496
- Sakurai, Y., Yoshida, N., Fujii, M. S., & Hirano, S. 2017, *MNRAS*, 472, 1677
- Schauer, A. T. P., Regan, J., Glover, S. C. O., & Klessen, R. S. 2017, *MNRAS*, 471, 4878
- Shakura, N. I., & Sunyaev, R. A. 1973, *A&A*, 24, 337
- Shapiro, S. L., & Teukolsky, S. A. 1983, *Black holes, white dwarfs, and neutron stars: The physics of compact objects* (Wiley)
- Stacy, A., Bromm, V., & Lee, A. T. 2016, *MNRAS*, 462, 1307
- Stone, J. M., Pringle, J. E., & Begelman, M. C. 1999, *MNRAS*, 310, 1002
- Sugimura, K., Coppola, C. M., Omukai, K., Galli, D., & Palla, F. 2016, *MNRAS*, 456, 270
- Sugimura, K., Hosokawa, T., Yajima, H., & Omukai, K. 2017, *MNRAS*, 469, 62
- Sugimura, K., Omukai, K., & Inoue, A. K. 2014, *MNRAS*, 445, 544
- Susa, H., Hasegawa, K., & Tominaga, N. 2014, *ApJ*, 792, 32
- Suzuki, T. K., & Inutsuka, S.-i. 2014, *ApJ*, 784, 121
- Tagawa, H., Umemura, M., Gouda, N., Yano, T., & Yamai, Y. 2015, *MNRAS*, 451, 2174
- Takeo, E., Inayoshi, K., Ohsuga, K., Takahashi, H. R., & Mineshige, S. 2018, *MNRAS*, arXiv:1705.05382
- Tanaka, T. L., & Li, M. 2014, *MNRAS*, 439, 1092
- Umeda, H., Hosokawa, T., Omukai, K., & Yoshida, N. 2016, *ApJ*, 830, L34
- Venemans, B. P., Findlay, J. R., Sutherland, W. J., et al. 2013, *ApJ*, 779, 24
- Visbal, E., Haiman, Z., Terrazas, B., Bryan, G. L., & Barkana, R. 2014, *MNRAS*, 445, 107
- Volonteri, M. 2012, *Science*, 337, 544
- Volonteri, M., & Rees, M. J. 2005, *ApJ*, 633, 624
- Volonteri, M., Silk, J., & Dubus, G. 2015, *ApJ*, 804, 148
- Wada, K. 2012, *ApJ*, 758, 66
- Wada, K., & Norman, C. A. 2002, *ApJ*, 566, L21
- Watarai, K.-y., Fukue, J., Takeuchi, M., & Mineshige, S. 2000, *PASJ*, 52, 133
- Willott, C. J., Delorme, P., Reylé, C., et al. 2010, *AJ*, 139, 906
- Wise, J. H., & Abel, T. 2007a, *ApJ*, 665, 899
- . 2007b, *ApJ*, 671, 1559
- Woods, D. T., Klein, R. I., Castor, J. I., McKee, C. F., & Bell, J. B. 1996, *ApJ*, 461, 767
- Wu, X.-B., Wang, F., Fan, X., et al. 2015, *Nature*, 518, 512
- Yajima, H., & Khochfar, S. 2016, *MNRAS*, 457, 2423
- Yajima, H., Nagamine, K., Zhu, Q., Khochfar, S., & Dalla Vecchia, C. 2017, *ApJ*, 846, 30
- Yoshida, N., Omukai, K., & Hernquist, L. 2008, *Science*,

321, 669

Yoshida, N., Omukai, K., Hernquist, L., & Abel, T. 2006, ApJ, 652, 6

Yuan, F., Bu, D., & Wu, M. 2012, ApJ, 761, 130

APPENDIX A: INNER AND OUTER SOLUTIONS OF ANALYTICAL MODEL

Our model consists of an outer dynamically equilibrium distribution (Sec. A1) and an inner viscous Keplerian disc (Sec. A2), which are connected at the centrifugal radius. Below, we describe the outer and inner solutions in this order.

A1 Outer dynamically equilibrium distribution

Here, we describe an outer dynamically equilibrium distribution connected to a homogeneous medium (Papaloizou & Pringle 1984). We assume that the gas is isothermal and that the angular momentum $j = j_\infty$ everywhere.

We start by describing the equation for the dynamical equilibrium between the gravity, pressure gradient and centrifugal force,

$$-\frac{1}{\rho}\nabla p - \left(\frac{GM_{\text{BH}}}{r^2}\right)\hat{r} + \left(\frac{j_\infty^2}{R^3}\right)\hat{R} = 0, \quad (\text{A1})$$

where \hat{r} and \hat{R} are the unit vectors in the r and R directions, respectively. Using the isothermal equation of state, $p = c_s^2\rho$, Eq. (A1) can be rewritten as

$$\nabla \left(c_s^2 \ln \rho - \frac{GM_{\text{BH}}}{r} + \frac{j_\infty^2}{2R^2} \right) = 0. \quad (\text{A2})$$

Then, imposing the outer boundary condition of constant density except near the pole, i.e., $\rho \rightarrow \rho_\infty$ as $r \rightarrow \infty$ with finite θ , we obtain

$$\begin{aligned} \rho &= \rho_\infty \exp \left[\frac{GM_{\text{BH}}}{rc_s^2} - \frac{j_\infty^2}{2R^2c_s^2} \right] \\ &= \rho_\infty \exp \left[\frac{r_{\text{B}}}{r} - \frac{R_{\text{c},\infty}r_{\text{B}}}{2R^2} \right], \end{aligned} \quad (\text{A3})$$

where we have used $r_{\text{B}} = GM_{\text{BH}}/c_s^2$ and $R_{\text{c},\infty} = j_\infty^2/GM_{\text{BH}}$ in the second equality. The density ρ rapidly decreases towards the pole, i.e., as $R \rightarrow 0$, due to the assumed constant angular momentum.

The density profile corresponds to that of a thin disc at $R \ll r_{\text{B}}$. Near the equatorial plane, where $r_{\text{B}}/r = r_{\text{B}}/(\sqrt{R^2 + z^2}) \approx (r_{\text{B}}/R)(1 - z^2/2R^2)$, we can approximate Eq. (A3) as

$$\rho \approx \rho_{\text{eq}}(R) \exp \left[-\frac{z^2}{2H_s^2} \right], \quad (\text{A4})$$

with the equatorial density,

$$\rho_{\text{eq}} = \rho_\infty \exp \left[\frac{r_{\text{B}}}{R} - \frac{R_{\text{c},\infty}r_{\text{B}}}{2R^2} \right], \quad (\text{A5})$$

and the scale height,

$$H_s = \frac{c_s}{\Omega_{\text{K}}}. \quad (\text{A6})$$

At $R \ll r_{\text{B}}$, where the aspect ratio $H_s/R = (R/r_{\text{B}})^{1/2}$ is small, the majority of gas is confined to a layer with

$|z| \lesssim O(H_s)$. In such layer, the approximate form of Eq. (A4) is valid and the integration in the z -direction yields the expression for surface density,

$$\Sigma \approx \sqrt{2\pi}H_s\rho_{\text{eq}}(R), \quad (\text{A7})$$

which can be rewritten as Eq. (9) with Eq. (A4). Note that ρ_{eq} has its maximum at $R = R_{\text{c},\infty}$, as the pressure gradient is balanced with the gravity at $R > R_{\text{c},\infty}$ but with the centrifugal force at $R < R_{\text{c},\infty}$.

A2 Inner viscous Keplerian disc

Next, we describe a thin Keplerian disc extended towards the BH (e.g., Shakura & Sunyaev 1973; Kato et al. 1998; Frank et al. 2002). Through the disc, the steady accretion is driven by the angular momentum transport via the α -type viscosity. Again, we assume the isothermal gas.

The gas distribution is governed by the following equations. Since the disc is vertically hydrostatic, the z -dependence of density is the same as Eq. (A4) and thus the relation between ρ_{eq} and Σ is given by Eq. (A7) (though ρ_{eq} is different from Eq. A5). Radially, the gravity is balanced with the centrifugal force with angular velocity

$$\Omega = \Omega_{\text{K}}. \quad (\text{A8})$$

The vertically-integrated mass conservation equation can be written as

$$2\pi R v_{\text{R}} \Sigma = -\dot{M}, \quad (\text{A9})$$

with the accretion rate $\dot{M} (> 0)$. Finally, the vertically-integrated angular momentum conservation equation is given by

$$-\dot{M}R^2\Omega_{\text{K}} + 3\pi R^2\nu\Sigma\Omega_{\text{K}} = \dot{J}, \quad (\text{A10})$$

with the net angular momentum flux $\dot{J} (= \text{const})$. Note that we have used Eqs. (A8) and (A9) to obtain Eq. (A10). Finally, we adopt the α -type viscosity

$$\nu = \frac{\alpha \gamma c_s^2}{\Omega_{\text{K}}}, \quad (\text{A11})$$

which is the same as Eq. (8) with $f = 1$.

The structure of the disc is uniquely determined once c_s , α , \dot{M} and \dot{J} are given. Here, \dot{J} can be determined from the inner boundary condition: we impose the torque-free condition, i.e., the second viscous stress term in Eq. (A10) is set to zero, at the inner boundary where the first advection term, which is proportional to $R^{1/2}$, is also small.⁵ Thus, neglecting \dot{J} in the right-hand side of Eq. (A10), we finally obtain $\dot{M} = 3\pi\nu\Sigma$ (Eq. 10). For given \dot{M} , with Eq. (10), as well as Eqs. (A7), (A8), (A9) and (A11), we can straightforwardly derive

$$\rho_{\text{eq}} = \frac{GM_{\text{BH}}\dot{M}}{3\sqrt{2\pi^3}\alpha\gamma c_s^3 R^3} \propto R^{-3}, \quad (\text{A12})$$

$$v_{\text{R}} = -\frac{3\alpha\gamma c_s^2\sqrt{R}}{2\sqrt{GM}} \propto R^{1/2}, \quad (\text{A13})$$

⁵ In the literature, the torque-free boundary condition is often imposed at the innermost stable circular orbit (ISCO), which is located at $6GM_{\text{BH}}/c^2$ in the case of Schwarzschild BHs.

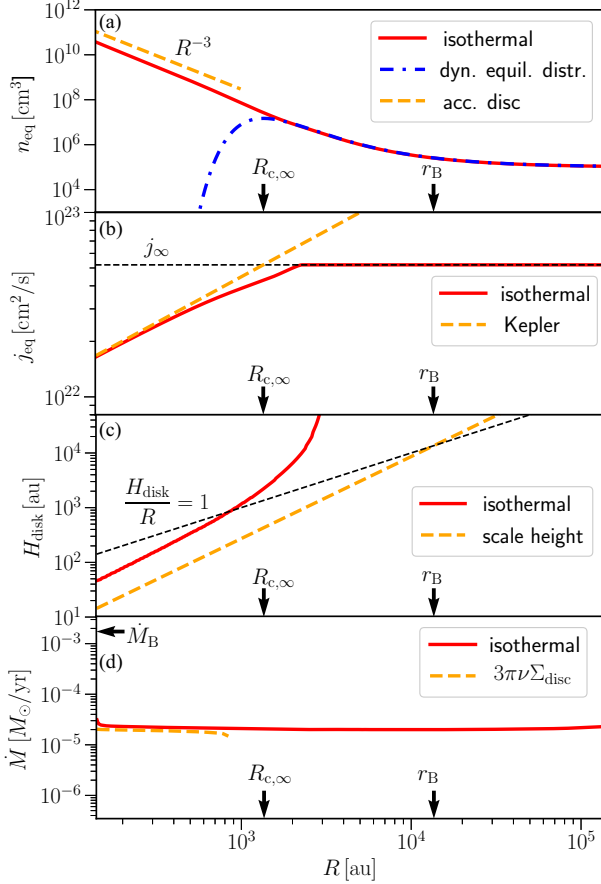


Figure B1. The radial profiles of the gas in the isothermal accretion from a medium with constant angular momentum. Each panel represents (a) equatorial density, (b) equatorial specific angular momentum, (c) disc height and (d) net accretion rate. The case with $\alpha = 0.01$ and $R_{c,\infty} = 0.1 r_B$ is shown.

and

$$v_\phi = \sqrt{\frac{GM}{R}} \propto R^{-1/2}, \quad (\text{A14})$$

which motivate the inner boundary conditions adopted in our simulations (see Sec. 2).

APPENDIX B: NUMERICAL CONFIRMATION OF ANALYTICAL MODEL

To confirm the validity of our analytical model, we compare the analytical results with the numerical ones, by performing simulations in the equivalent settings.

Here, we start the simulation from the dynamical equilibrium distribution with $j = j_\infty$ everywhere (Eq. A3). For the computational reason, if the density ρ is initially below the floor density, we set ρ at the floor density and $j = 0$. We assume the isothermal gas at $T = 10^4$ K. Here, we adopt $\alpha = 0.01$ or 0.1 and $R_{c,\infty}/r_B = 0.03, 0.04, 0.05, 0.06, 0.08, 0.14, 0.2$ or 0.3 . We stop the calculation when the time variation of \dot{M} becomes sufficiently small. For the simulations presented here, we limit j to below j_∞ , as in the lowest angular momentum ($R_{c,\infty}/r_B = 0.03$) run in Sec. 3. The rest

of the numerical method is the same as that described in Sec. 2.

To begin with, let us investigate the gas distribution, focusing on the case with $\alpha = 0.01$ and $R_{c,\infty} = 0.1 r_B$. In Fig. B1, the profiles of several quantities obtained at the end of the simulation are compared with the analytical model. First, Fig. B1(a) shows the equatorial density n_{eq} . It agrees excellently with that of the dynamically equilibrium distribution (Eq. A5) at $R > R_{c,\infty}$, while its R dependence of $\propto R^{-3}$ is the same as the viscous Keplerian disc at $R < R_{c,\infty}$. Second, in Fig. B1(b), the equatorial specific angular momentum j_{eq} is presented. It is equal to the asymptotic value of j_∞ at $R \gg R_{c,\infty}$, while it is close to the Keplerian profile $j_K = R^2 \Omega_K$ at $R \ll R_{c,\infty}$. However, the agreement is not perfect around $R_{c,\infty}$, because the non-negligible pressure gradient reduces j compared with j_K . Recall that we here impose the upper limit at j_∞ by removing j otherwise accumulated just outside the outer edge of the disc. Third, in Fig. B1(c), we show the disc height H_{disc} at which ρ drops to one hundredth of ρ_{eq} . The disc is thin, i.e., $H_{\text{disc}}/R \lesssim 1$, at $R \lesssim R_{c,\infty}$, but it rapidly swells up at $R > R_{c,\infty}$. For the thin part, the relation $H_{\text{disc}} \approx 3H_s$ holds, consistent with the vertical dependence of ρ in Eq. (A4). Finally, in Fig. B1(d), we plot the net accretion rate over the entire solid angle,

$$\dot{M} = 2 \int_0^{\pi/2} \rho(r, \theta) v_r(r, \theta) 2\pi r \sin \theta d\theta. \quad (\text{B1})$$

It is constant with R , consistent with the steady accretion. For the range where the disc is thin ($H_{\text{disc}}/R < 1$), we also plot $3\pi\nu\Sigma_{\text{disc}}$ (see Eq. 10), using the disc surface density, $\Sigma_{\text{disc}} = \int_{-H_{\text{disc}}}^{H_{\text{disc}}} \rho(R, z) dz$, obtained from the simulation. It agrees surprisingly well with \dot{M} , implying that the accretion is indeed driven by the angular momentum loss. In summary, the numerical result is fully consistent with the analytical model.

As expected from the above agreement in the gas distribution, the analytical model can nicely reproduce the numerical accretion rates for the various sets of the parameters, as shown in Fig. 7. In all cases, the difference between the analytical and numerical results is less than a factor of three, ensuring the qualitative validity of the analytical model.

In order to check the effect of imposing the upper limit on j , we have made test calculations without the limit. In such a case, we have found that j is accumulated outside the outer edge of the disc, which gradually expands as the accumulation proceeds. The effective enhancement of j makes \dot{M} smaller, especially in the case with smaller $R_{c,\infty}$. As a result, the rapid increase of \dot{M} with decreasing $R_{c,\infty}$, as seen in Fig. 7, disappears. The effect of imposing the limit is insignificant for the case with $R_{c,\infty} \gtrsim 0.1 r_B$, where its impact on \dot{M} is at most 30 percent.

Finally, we briefly mention the effect of changing $\tilde{\Omega}$, which regulates the region where the viscosity works (Eq. 8). In the test runs with $\tilde{\Omega}$ different from the fiducial value of 0.8 (with $\alpha = 0.01$ and $R_{c,\infty} = 0.1 r_B$), we have seen that \dot{M} increases with decreasing $\tilde{\Omega}$ and becomes three times larger in the case of $\tilde{\Omega} = 0.6$. While the quantitative determination of \dot{M} is affected by the specific prescription of viscosity, we do not expect it qualitatively changes the conclusion of this work.

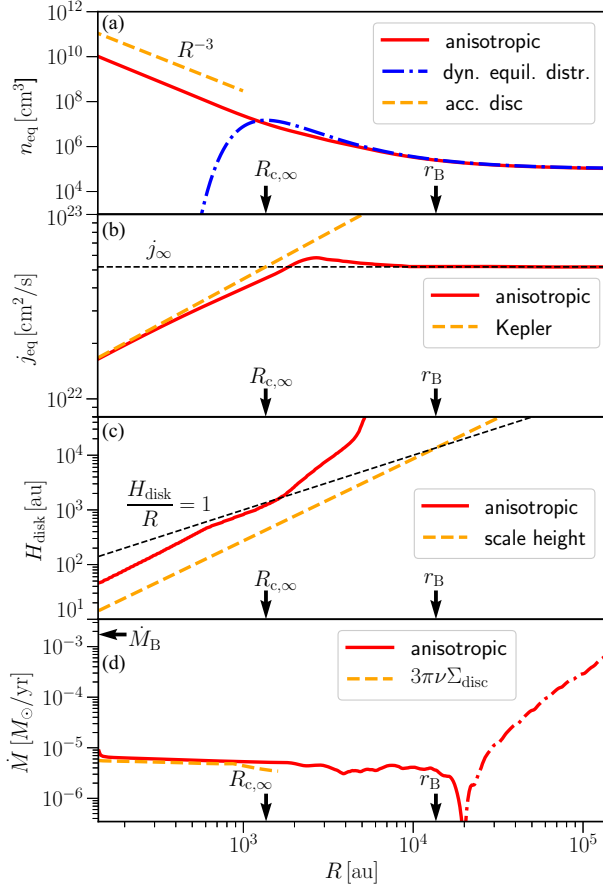


Figure C1. Same as Fig. B1 but for the anisotropic radiation run with $\alpha = 0.01$ and $R_{c,\infty} = 0.1 r_B$. In panel (d), solid (dot-dashed) lines show a positive (negative) value.

APPENDIX C: EQUATORIAL GAS PROFILE IN ANISOTROPIC RADIATION RUN

Here, we show the equatorial gas profile in the anisotropic radiation run in Sec. 3.1, where $\alpha = 0.01$ and $R_{c,\infty} = 0.1 r_B$. We average the profiles of n_{eq} , j_{eq} , H_{disc} and \dot{M} for the last 3×10^5 yr with the time intervals of 2×10^3 yr (using 150 snapshots in total) and plot them in Fig. C1 in the same way as Fig. B1. In each panel, the profile in the anisotropic radiation run generally agrees with that considered in the analytical model.

Let us make several remarks on Fig. C1. First, in Fig. C1(c), while H_{disc} is smaller than the assumed 45° shadow and ionizing photons do not reach the disc surfaces at $R \lesssim 0.5 R_{c,\infty}$, $H_{\text{disc}}/R \sim 1$ at $R \sim R_{c,\infty}$ because H_{disc} is determined by the shadow angle there. Second, in Fig. C1(b), j_{eq} exceeds j_∞ at $R \gtrsim R_{c,\infty}$ due to the accumulation of j transported from the inside. Note that, for simplicity, we do not impose the upper limit on j in this run. Recall, however, that we have seen in Appendix B that the imposition of the upper limit does not significantly affect \dot{M} for the case with $R_{c,\infty} \gtrsim 0.1 r_B$. Finally, in Fig. C1(d), the net accretion rate \dot{M} is roughly constant at $R \lesssim r_B$ but largely varies outside, corresponding to the small time variation remaining even near the end the simulation, as seen in Fig. 2(a).

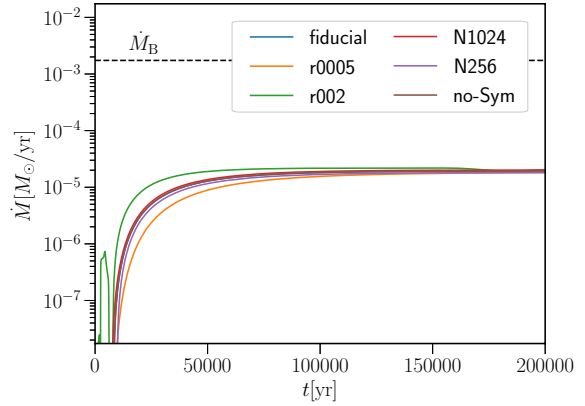


Figure D1. Same as Fig. 2(a) but for the fiducial case in Sec. B with different numerical configurations (see text). The lines for the fiducial, no-Sym and N1024 runs are overlapped with each other.

APPENDIX D: DEPENDENCE ON NUMERICAL CONFIGURATIONS

To examine the dependence of our results on the numerical configuration, we rerun the simulation of the fiducial case in Appendix B with different numerical configurations. Until now, we adopt the following configurations: the inner boundary is at $r_{\text{in}} = 10^{-2} r_B$; the number of grids is $N_r \times N_\theta = 512 \times 144$; and the range of θ is $0 < \theta < \pi/2$ under mid-plane symmetry. However, we here replace one of them as: $r_{\text{in}} = 5 \times 10^{-3} r_B$ (r0005 run); $r_{\text{in}} = 2 \times 10^{-2} r_B$ (r002); $N_r \times N_\theta = 1024 \times 288$ (N1024); $N_r \times N_\theta = 256 \times 72$ (N256); and $0 < \theta < \pi$ without mid-plane symmetry (no-Sym).

Fig. D1 shows the time evolution of \dot{M} . While there are some differences in the early stage ($t \lesssim 5 \times 10^4$ yr), all the runs give practically the same value in the end. Note that \dot{M} is not affected by the assumption of mid-plane symmetry, while the non-symmetric modes are known to be evident in the former simulations of the accretion to active galactic nuclei (e.g., Stone et al. 1999). Note also that we find considerable deviations between the cell-centered and cell-boundary mass fluxes in the run with the reduced grids (N256), although \dot{M} is not affected by such deviations. In summary, our simulation results of \dot{M} are apparently independent of the numerical configuration in the case without radiation feedback.

In this work, we consider the radiation feedback, as well as the angular momentum. For the non-rotating case with radiation feedback, Sugimura et al. (2017) have shown that the resolution dependence is insignificant with the current numerical configuration. Thus, we expect that the dependence of our results on the numerical configuration in the case with both angular momentum and radiation feedback is also modest.

APPENDIX E: GRAVITATIONAL STABILITY OF DISCS

In the cases studied in this work, the disc is always gravitationally stable according to the Toomre criterion, i.e., the Toomre Q defined as

$$Q = \frac{\kappa_{\Omega} c_s}{\pi G \Sigma}, \quad (\text{E1})$$

with the epicyclic frequency $\kappa_{\Omega} = ((2\Omega/R)d/dR(R^2\Omega))^{1/2}$, is larger than unity. In the following, to see under what conditions the disc becomes gravitationally unstable, we derive the parameter dependence of Q based on the analytical model in Sec. 4.1.

Using Σ of the analytical model obtained from Eqs. (10) and (12), we can rewrite Eq. (E1) as

$$Q \approx \frac{3c_s^2 r_B}{2\pi^{3/2} G R_{c,\infty}^3 \rho_{\infty}} \exp\left[-\frac{r_B}{2R_{c,\infty}}\right], \quad (\text{E2})$$

where the R and α dependences are canceled out. This yields $Q \sim 10^3$ when $M_{\text{BH}} = 10^3 M_{\odot}$, $n_{\text{H},\infty} = 10^5 \text{ cm}^{-3}$ and $R_{c,\infty} = 0.1 r_B$, consistent with the simulation results. With the Jeans length $\lambda_J = \sqrt{\pi c_s^2 / G \rho}$, Eq. (E2) can be further rewritten as $Q \approx 0.3 (r_B / R_{c,\infty})^3 (\lambda_J / r_B)^2 \exp[-r_B / 2R_{c,\infty}]$. This suggests that Q could be less than unity, i.e., the disc could be gravitationally unstable, in the case with smaller λ_J / r_B ($\propto M_{\text{BH}}^{-1} n_{\text{H},\infty}^{-1/2}$) and/or $R_{c,\infty} / r_B$.